GEOLOGICAL SURVEY OF CANADA

OPEN FILE 2771

Investigation of the properties of the Saskatchewan lithosphere using teleseismic waves

R.M. Ellis, Z. Hajnal

1993

Natural Resources Canada
Ressources naturelles Canada

Canada

Saskatchewan

L'ENTENTE DE PARTENARIAT SUR
L'EXPLOITATION MINÉRALE 1990 - 1995

PARTNERSHIP // ASSOCIATION

PARTNERSHIP AGREEMENT ON MINERAL
DEVELOPMENT 1990 -1995

Canada

GEOLOGICAL SURVEY OF CANADA

OPEN FILE 2771

INVESTIGATION OF THE PROPERTIES OF THE SASKATCHEWAN LITHOSPHERE USING TELESEISMIC WAVES[1]

R.M. Ellis[2] and Z. Hajnal[3]

NOVEMBER 1993

---

[1] Contribution to Canada-Saskatchewan Partnership Agreement on Mineral Development (1990-1995), a subsidiary agreement under the Canada-Saskatchewan Economic and Regional Development Agreement.

[2] Department of Geophysics and Astronomy, University of British Columbia, Vancouver, B.C. V6T 1Z4

[3] Department of Geological Sciences, University of Saskatchewan, Saskatchewan, Saskatchewan S7N 0W0

Investigation of the Properties
of the
Lithosphere Using Teleseismic Waves

Report for Energy, Mines and Resources Canada and Cameco Corporation

Contracting Agency: Supplies and Services Canada
(Contract No. 23235-1-3062/01-SS)

Principal Investigator:
R. M. Ellis
Department of Geophysics and Astronomy
University of British Columbia
Vancouver, B.C.
V6T 1Z4

Research Assistants: J. Amor
N. Dotzev
R. D. Meldrum
T. Mulder

Granting Agency: Cameco Corporation

Principal Investigator:
Z. Hajnal
Department of Geological Sciences
University of Saskatchewan
Saskatoon, SK
S7N 0W0

May 1992

Introduction

Although there have been reports of earlier diamond finds in Saskatchewan, the documentation has been limited (Gent, 1992). The current activity stems from the discovery of a diamondiferous kimberlite body ~30 km northwest of Prince Albert which was reported by Monopros in late 1988. Subsequently, the presence of 16 kimberlite pipes has been reported, over 700,000 hectares have been staked, and diamonds as large as ~4 mm have been found. Sections of the geological community (e.g. Collerson et al., 1990) are now making efforts to understand the occurrence of the kimberlite bodies in relation to the tectonic evolution of this area and thus determine where kimberlites may exist in the buried basement. This program has a similar focus.

Diamonds - Some Basics

Kirkley et al. (1992) have reviewed our current knowledge of diamonds from which we abstract some of the principal observations.

Until recently, the genetic association between the diamonds and and their host rocks has been unresolved. A series of studies have now determined the ages of diamonds and the emplacement age of the kimberlite pipes with which they are associated (Richardson et al., 1984; Richardson, 1986; Richardson et al., 1990). Key results from these studies are as follows:

(i) Diamonds are usually much older than the kimberlite or lamproite that brought them to the surface;
(ii) Diamond ages determined are between ~3300 and 990 Myr, i.e. they are old and have formed during a major part of the earth's history;
(iii) Diamonds are stored at depth for an extended period of time before being transported to the surface - emplacement ages are as recent as 100 Myr;
(iv) Diamonds of different ages within one pipe are possible which suggests two different mantle sources.

In view of the above relationships, the best explanation of the occurrence of diamond in kimberlites and lamproites is that the diamonds formed in xenolithic materials which are older than the kimberlite or lamproite which carried them to the surface. Stability constraints suggest ascent rates of 10 to 30 km per hour (Eggler, 1989).

Two types of diamondiferous xenoliths have been found, eclogite and peridotite with the eclogite dominating numerically by a factor of about five. Meyer (1985) has evaluated the studies of pressure and temperature at which diamonds have formed and concludes that the peridotitic diamonds form in the depth range 150 km to 200 km with the eclogitic diamonds at greater depths; Moore and Gurney (1985) have found that some of the latter may have formed at depths greater than 300 km. Formation at these depths is consistent with the observation that kimberlites are never found in oceanic environments or young mountain belts but within the cratons which have thick lithospheres and low temperature gradients.

On the basis of these physical parameters, Haggerty (1986) has constructed a model for genesis of diamonds (Fig. 1). On a craton bounded by mobile belts he sketches isotherms and the graphite-diamond stability curves. In this schematic, he infers that the eclogite is derived from ocean basalts which have been subducted beneath the continent. The most significant section in this diagram is the region bounded by the 1200^0 C isotherm and the diamond-graphite stability curve. It is here that diamonds can be preserved. Kimberlite pipe K1 is ideally situated over the thickest portion of the craton and would be likely to contain diamonds, if other factors, e.g. a rapid ascent rate, are favorable; K2 on the margin of the craton would only contain diamonds if the temperature gradient were low; and K3 would be barren. To explain the off-craton diamondiferous Argyle and Ellendale lamproite diatremes of Australia, he proposes a complex "plumbing system" as exemplified by pipe L1.

For kimberlites to reach the surface requires availability of fractures from the base of the lithosphere to the surface. Generation of these is not well understood although several hypotheses have been proposed, e.g. crack propagation by magmatic fracturing (Eggler, 1989), crustal thinning associated with major plate movements (Dawson, 1989), and the development of monoclinal axes or basin hinges as the result of compression and loading (Gent, 1992).

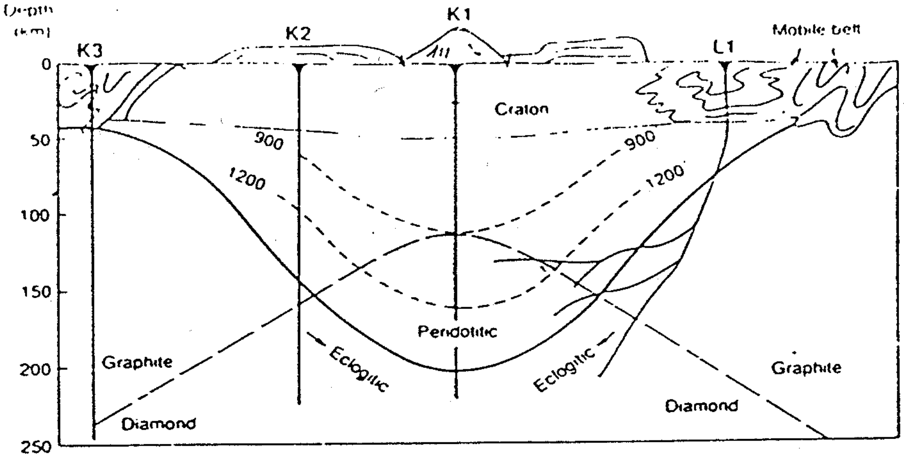

Figure 1. Model for the genesis of diamond simplified from Haggerty (1986). The stable craton and subcratonic areas are 50 km to 200 km thick and are bounded by mobile belts. Note the stability area for diamonds bounded by the diamond-graphite stability curve and the 1200° C isotherm (from Kirkley et al., 1992).

Application of Earthquake Seismology

As outlined in the previous section, lithospheric thickness is a key parameter in the diamond exploration problem. Further, data on the stress field in the geological past may have important implications for the transport of the diamonds to the surface by the kimberlites or lamproites. In both cases, earthquake seismology can aid our understanding. The lithospheric thickness can be investigated by the analysis of body wave traveltimes and waveforms and mantle anisotropy can be determined from the polarization of the SKS phase. Silver and Chan (1988) suggest that the observed anisotropy in the Canadian shield can be interpreted in terms of the stress field at the end of the Archean.

Objectives/Program

As outlined in the Project Identification and Annual Plan, the overall approach is to carry out a broad scale mapping of the crust and lithosphere in Saskatchewan southward from the Glennie Lake domain. The boundaries of this domain have been tentatively mapped beneath the Phanerozoic cover using potential field data (Morel-à-l'Hussier, 1990). This is to be done by deploying 3-component digital seismographs to record teleseisms from which the properties of the crust and mantle can then be extracted.

In particular, the techniques to be applied are as follows:

(i) Traveltime variations - these provide variations in the thickness/velocity of the crust and lithosphere beneath the array.

(ii) Receiver function analysis - it is well established that this technique which examines the amplitudes and arrival times in the P-coda can provide the shear velocity structure to depths of at least 60 km even where the surface structure is complex (Owens et al., 1987; Cassidy, 1991). In central Saskatchewan where there is little topography or near surface structure, we should expect to obtain the shear structure to depths near 100 km provided that distinct boundaries exist. Paulssen (1988) claims to have detected the 670 km discontinuity by this procedure. This technique, as well as providing information itself, will be used to to place constraints on the interpretation of (i).

(iii) SKS anisotropy - particle motions of this phase, which starts from the core-mantle boundary as a linearly polarized waveform, yield the azimuthal anisotropy of the upper mantle and hence the preferred orientation of the minerals. This can be interpreted in terms of the deformational processes.

This study was planned in 3 phases:

(i) 1991-92: Feasibility tests, both scientific and technical. For a complete description, see plans for current fiscal year. Only if the results of this program are encouraging would the second and third phases be considered.

(ii) 1992-93: Full-scale field program with ~12 seismograph stations deployed for 8 to 12 months and initiation of analysis.

(iii) 1993-94: Analysis and interpretation.

Program for 1991-92 Fiscal Year

As indicated above, this program is a feasibility study. Following laboratory tests both in Ottawa and Vancouver, an initial field phase of 2 months was proposed during which four seismographs would be deployed with one at each of the following sites: (i) on the exposed Glennie Lake domain; (ii) on the Glennie Lake domain where there is Phanerozoic cover; (iii) at the Saskatoon vault where there are excellent test conditions; and (iv) at a site well-removed from the orogen. During this stage the technical problems were to be tackled; these seismographs have not previously been used to record teleseisms nor in a high noise level sedimentary environment. Following this, two to four additional seismographs were to be deployed for several months to acquire a minimum data set.

The overall objectives of this initial experiment are : (i) to allow definition of technical problems; (ii) to provide sufficient data to test each of the techniques and to evaluate whether anomalies exist; and (iii) to provide an improved estimate of the time period and number of stations required to provide an adequate data set for a full-scale analysis program.

Testing and Recording Parameters

Preliminaries

In late May, R.D. Meldrum visited Ottawa for familiarization with the Scintrex PRS-4 recorders and associated LithoSEIS software, and to initiate investigation of the appropriate recording parameters. Four recorders and a Field Service Unit were shipped to Vancouver at this time for further tests and also modifications. Two modifications were required:

(i) To make full use of the Guralp broadband capabilities for teleseimic deconvolution studies required that the passband of the PRS-4 recorders be extended from 0.5 to 0.05 Hz. The modifications required and the associated signal channel offset problems are documented in Appendix A. We note that broadband seismometers are desirable as effects of small scale scatters can be minimized and they provide the capability to detect gradient boundaries.

(ii) To obtain traveltime residuals requires accurate timing (to within several 10's of ms) at each station. This was achieved by recording 20 s of the radio time signal WWVB on the hour at 7 hour intervals (later 13 hours) during the experiment which allowed timing to be known to within 10 ms between clock ratings. This required that the input filter removed from channel 4 to provide an unconditioned input for calibration reference signals. The details of this modification to the PRS-4 are provided in Appendix A and the timing techniques used are documented in Appendix B.

Installation

Three recorders were installed in early July, a fourth in early August, and 4 more in early September; further, a second recorder was installed at the University of Saskatchewan seismic vault specifically to monitor the SKS phase. The final group of 5 recorders were not available until completion of a Lithoprobe refraction program. The station locations are shown in Fig. 2 and the detailed station parameters, including period of operation, are provided in Table 1. The latitudes, longitudes and elevations were obtained using a satellite location system (GPS). The depth and traveltime to the Precambrian basement were obtained from well logs.

Where concrete pads or bedrock outcrops were available, the seismometers were placed directly on these surfaces. Otherwise, Guralp seismometers were placed in concrete-lined containers and buried while Mark L4-C seismometers were buried directly. Generally the seismographs are in abandoned farm buildings; the exceptions are USK, which is in the University of Saskatchewan seismic vault, and DLK where a school building is used.

Recording parameters for the eight stations focussed on recording the P onset and the first minute of its coda and are as follows (the 'standard configuration'): sampling rate - 50/s; passband: 0.05 - 5 Hz; recording 30 s before trigger and 60 s after trigger. Trigger characteristics: effectively bandpass 0.6 - 2 Hz, STA - 2.54 s, LTA - 102.2 s, trigger ratio = 6. A broadband recording with these recording parameters is shown in Fig. 3.

Recording of SKS presents several complications. Firstly, the SKS arrives ~10 min after the P onset. Since the PRS recording is triggered by the P onset and the lowest sample rate for which an effective trigger can be designed is 30 Hz, the number of earthquakes which can be recorded is severely limited; for 15 min of data, the total number of events is 17. Secondly, although the SKS phase initially appears at $\Delta \sim 62^0$, it is only readily observable beyond 84^0, where it arrives significantly before S, out to 110^0 by which time the amplitude has significantly decreased. Unfortunately the initial P phase, on which the seismograph triggers, rapidly decreases in amplitude beyond 80^0 and effectively disappears in the range 95^0 - 100^0 (Fig. 4). Thus by operating with a triggered system, we are effectively limiting ourselves to observing SKS from a restricted distance range. The trigger ratio of the SKS recorder was initially set to 15 to avoid filling the memory with low signal-to-noise ratio events. When the SKS system was found to have missed an $M = 6.5$ earthquake at $\Delta = 95^0$ in India, the trigger was given a bias toward lower

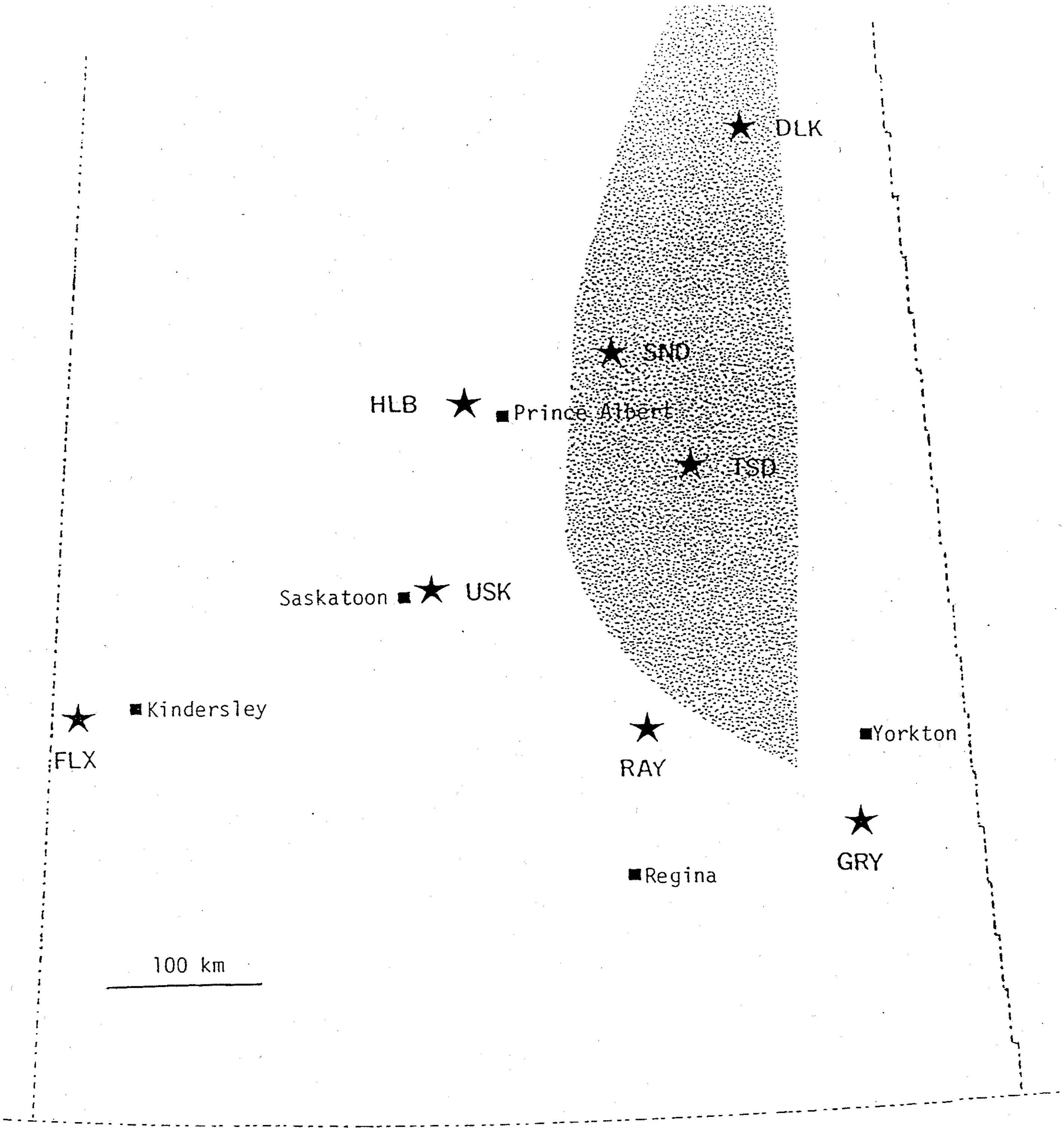

Figure 2. Location of seismic stations (stars) with interpreted extent of Glennie Domain shown as shaded region.

TABLE 1

STATION PARAMETERS

Station	Latitude	Longitude	Elevation (m)	PC (depth & time) (m)	(ms)	T_{corr} (ms)	Operation Dates 1991 1992	Detectors	Comments
DLK	54.9164	103.3760	374	0	0	62	8/06 - 1/09	Guralp	Deschambeault Lake
FLX	51.3800	109.6812	704	2146	646	406	7/03 - 1/04	Guralp	Flaxcombe
GRY	50.7088	102.5736	605	1640	474	294	9/10 - 1/07	L4-C	Grayson
HLB	53.3022	106.1309	506	1007	506	196	9/17 - 1/10	L4-C	Holbein
RAY	51.2969	104.4512	623	1725	515	331	9/02 - 1/06	Guralp	Raymore
SND	53.5777	104.6771	472	495	139	135	9/13 - 1/11	L4-C	Snowden
TSD	52.9008	103.9498	462	789	223	168	7/03 - 1/12	Guralp	Tisdale
USK	52.1961	106.3982	605	1785	526	329	7/02 - 1/12	Guralp	Saskatoon vault
							9/02 - 1/12	Guralp	SKS system

T_{corr} - vertical P-wave time correction to sea level; below sea level, the sediments are replaced by a 6 km/s section

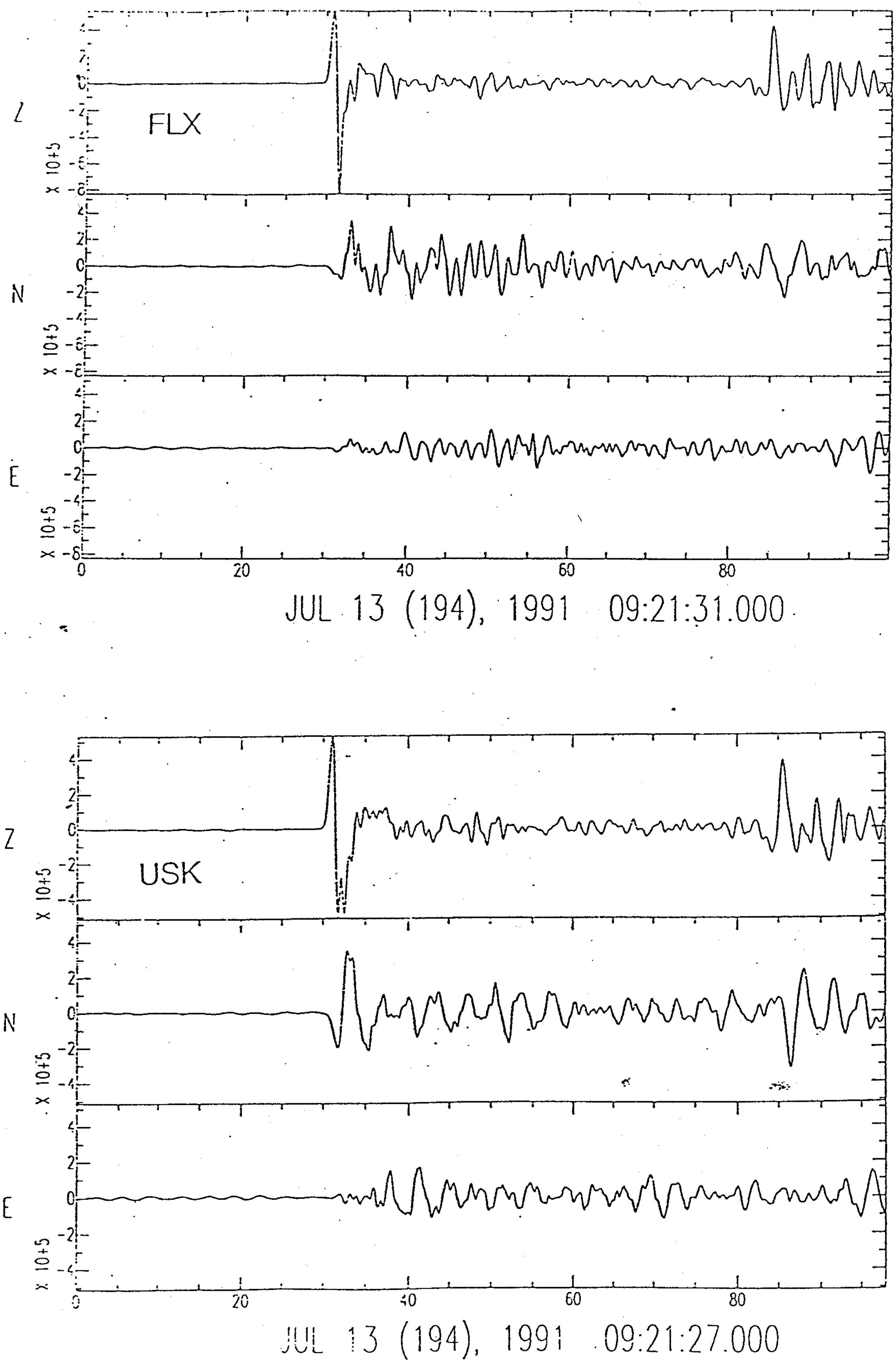

Figure 3. Three component broadband seismograms recorded at FLX and USK from an earthquake on the USSR - Afghanistan border. Magnitude is 6.4. Note the different signal characteristics between the two stations due to differential structure.

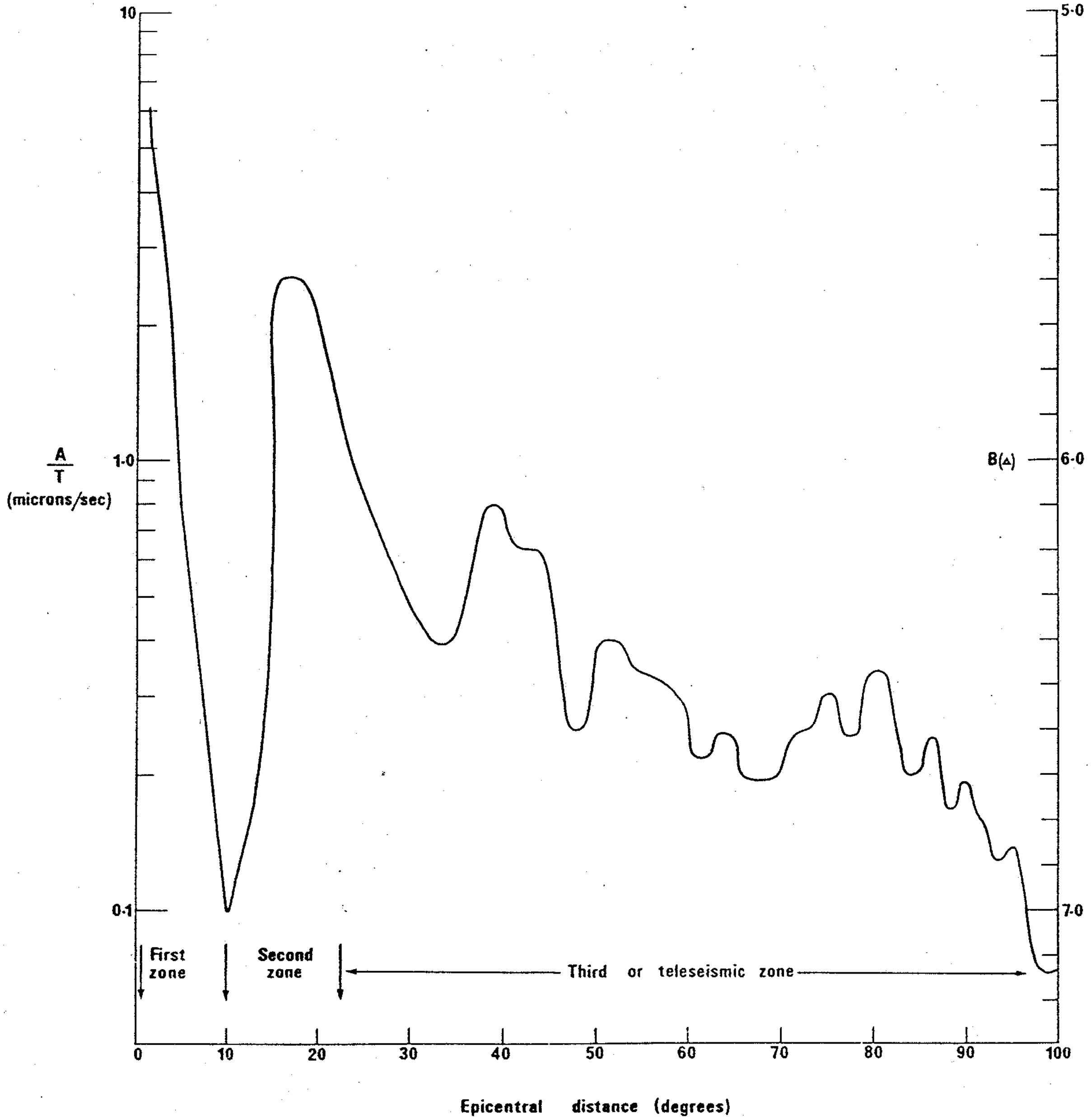

Figure 4. Expected values of A/T for a magnitude 6 earthquake. A/T for any other magnitude can be inferred from the figure by an appropriate change in scale. For example a magnitude 5.0 event would reduce the values shown by a factor of 10. Note the rapid decrease of A/T beyond 80 (from Davies, 1968).

frequency arrivals. Selection of trigger parameters is complicated by the 3 s microseismic background noise. As precise timing is not required in this application, WWVB was not recorded. The PRS clock is rated at deployment and recovery times and linear interpolation used to obtain approximate event times. If necessary, precision timing can be obtained by referencing corrected times for the P arrivals recorded on the standard configuration PRS at this site.

Recording parameters for the SKS system are presently as follows: sampling - 30/s; recording 30 s before and 900 s after trigger; Trigger characteristics: STA - 2.1 s, LTA - 85 s, ratio = 9.5. Other parameters are as for the standard configuration.

On-site amplitude and phase calibrations of all broad band seismographs were conducted using a precision oscillator stepped in frequency through the band of interest. The outputs of the seismometers were recorded on the PRS's as was the calibration reference signal. Plots of amplitude and the phase responses of the entire system including the PRS indicate no significant differences between channels. Details of the trigger parameters and calibrations are presented in Appendix A.

P-Wave Residual Investigation

No previous studies have been published showing P-wave residuals (i.e. $T_{obs} - T_{theor}$) in Saskatchewan. The earlier Canadian studies (Buchbinder and Poupinet, 1977; Wickens and Buchbinder, 1980) do not have data from within the province; the only constraints on their plots for this area (Fig. 5 and 6) are the residuals for FFC (Flin Flon) on the east and SES (Suffield) and EDM (Edmonton) on the west. We note that Buchbinder and Poupinet (1977) made elevation corrections for each station and required that the average residual for each earthquake be zero relative to the J-B traveltime tables; Poupinet (1978) used residuals from the ISC Bulletin obtained in the determination of epicentres by the J-B traveltimes. These different approaches and data sets result in different base levels which are harmonized in Fig. 6. These plots indicate a decrease of P-residuals from west to east across Saskatchewan by ~0.2 s, i.e. earlier arrivals. A variation of this size can readily accounted for by the change in thickness of the sedimentary cover without appealing to velocity variations at depth.

During our recording period, 266 earthquakes were recorded. From these, 84 teleseisms were found to be well-recorded at USK and at least one other station (i.e. ~3 per week) and are useful for P-residual analysis. These earthquakes and the stations at which they are recorded are listed in Appendix C and their distribution plotted in Fig. 7. It is noted that the earthquakes are clustered in two azimuths, ~300° and ~150°, i.e. from the Aleutian-Kachatka-Japan direction and from Central and South America. No significant difference exists between the average magnitudes of earthquakes found to be useful for analysis in the July-September and October-December recording periods.

Method

Systematic techniques have been developed to investigate structures beneath receiver stations using traveltime residuals (e.g Buchbinder and Poupinet, 1977; Babuska et al., 1984a, 1984b, 1987a, 1987b). These are designed to minimize effects such as velocity inhomogeneities in the source and deep mantle regions. For optimum results, a good representation of azimuths and epicentral distances in the teleseismic range is required. However, for our tests with this limited data set a simplified approach is used. We examine two groups of earthquakes, each from a limited distance and azimuth range, and determine all residuals with respect to the station USK.

To obtain the traveltime differences for each earthquake, the following procedures have been used:

(i) The seismograms are bandpass filtered 0.1 - 4 Hz and the broad band records converted to short period records by filtering.

(ii) Raw traveltime differentials are determined by cross-correlation of the onset P waveform of a base station, (for the data presented USK), with that of each of the other stations. The nominal correlation window is from 1 s before to 3 s after the estimated P onset. In general, this window length and position are adjusted based on the waveform characteristics to

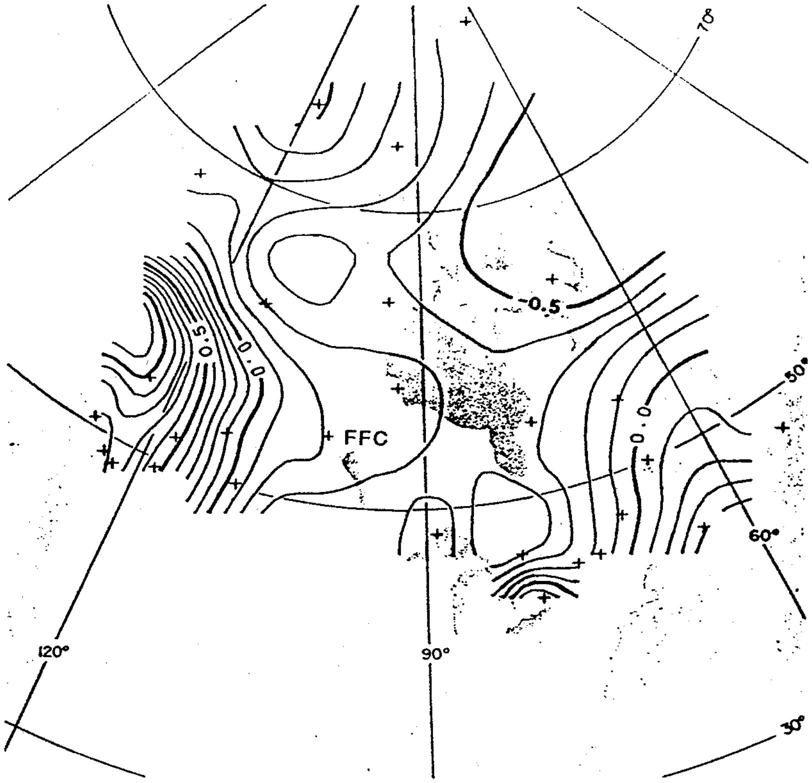

Figure 5. Contours of relative P residuals of Buchbinder and Poupinet (1977) [from Wickens and Buchbinder (1980)].

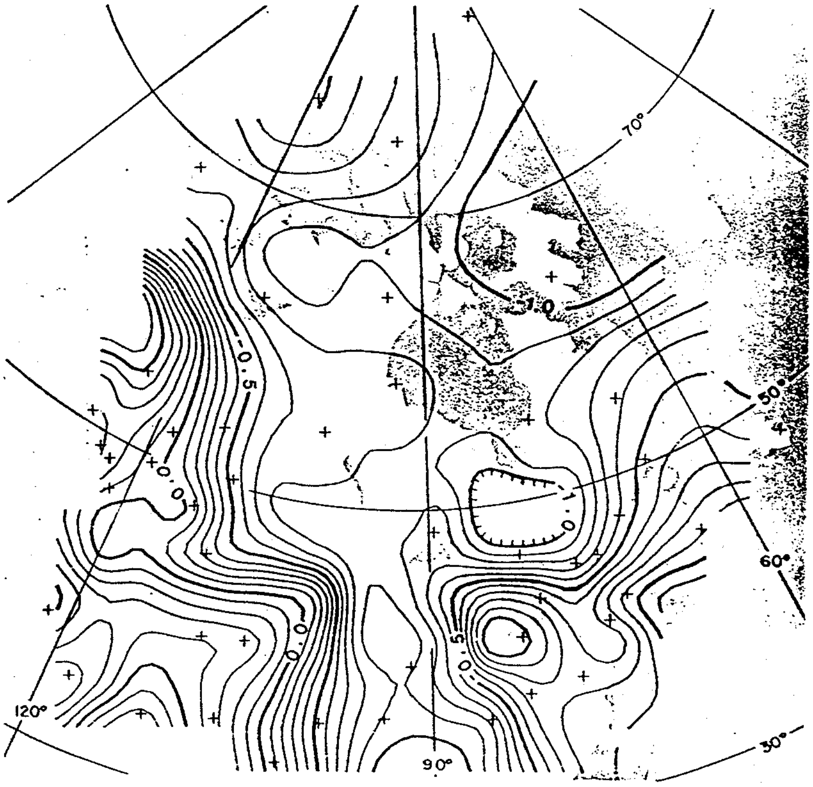

Figure 6. Contours of relative P residuals of Buchbinder and Poupinet (1977) augmented by data of Poupinet (1978). The difference in contour level is due to a baseline shift; for explanation, see text (from Wickens and Buchbinder (1980)].

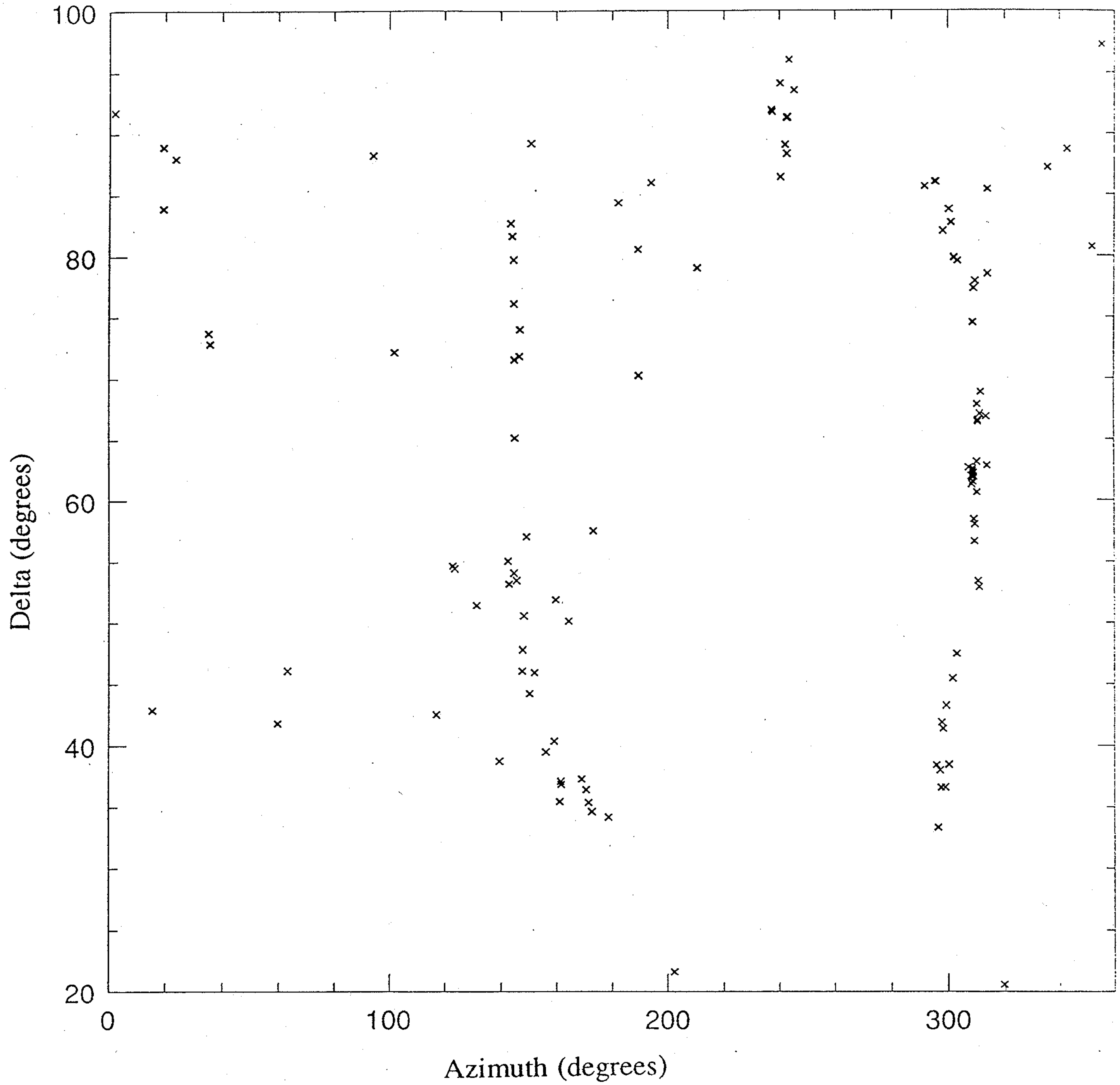

Figure 7. Distance and azimuth of earthquakes used for P residual analysis.

optimize the calculation. An estimate of the typical uncertainty in traveltime differences is 0.02 s.

(iii) Corrected traveltime differentials are then determined from the raw traveltime differentials by applying the corrections for the elevation and sedimentary thickness (Table 1), and the predicted traveltime differential based on Jeffreys-Bullen tables with elliptical corrections. By using traveltime differentials, effects of errors in source location and origin time are eliminated.

Examples of effects due to differential velocity structure are illustrated in Fig. 8a and 8b. (The horizontal axes for these and all other seismograms are in s.) The expected arrival times based on the J-B tables with corrections applied are marked as Pjb and the picked times as P. For the earthquake from the Kurile Islands (Fig. 8a), significant variations are evident; at USK, P and Pjb are identical while at FLX P leads Pjb and at TSD P lags Pjb. In contrast, the earthquake from the coast of Colombia (Fig. 8b) arrives significantly before the predicted time in all cases; the difference between Pjb and P is approximately the same at FLX and USK and decreases slightly at TSD. Clearly, significant residuals exist and they vary both between stations and with event location.

P-wave Residuals Results

To show that anomalies do exist, we present the traveltime residuals for two sets of earthquakes: (i) 15 earthquakes from Kurile Islands with $\Delta \sim 62^0$ and BAZ ~ 309^0, i.e. from the northwest direction ; and (ii) 8 earthquakes with $\Delta \sim 55^0$ and BAZ ~ 147^0 from South America, i.e. from the southeast (Fig. 9a and 9b). As shown in Fig. 8a and 8b for individual earthquakes, these two regions have quite different P-wave residuals although their distances and hence angles of incidence are similar. In Table 2 the results obtained in this preliminary investigation are shown.

Although the contours are only weakly constrained by the station density, several features are evident. For the earthquake suite arriving from the northwest, the key features of the residuals are the large negative residual at FLX and the large positive residual at TSD, i.e. FLX is early and TSD is late. For the earthquakes arriving from the southeast, the same pattern is evident at these stations but there are also very large positive residuals at RAY and GRY, the two stations in the southeast, and a very significant negative anomaly at DLK. Clearly these traveltime differentials imply very large structural variations at depth. In particular, the stations GRY, RAY and TSD, experience large time delays for arrivals from the southeast. We note that for earthquakes in this distance range the angle of incidence at Moho depths is ~30^0. Thus the rays from the two earthquakes are sampling quite different regions of the lithosphere at depth.

To put these anomalies in context, it is useful to arbitrarily assign the residuals to various components of the lithospheric column. Based on nominal values for velocity and thickness parameters, a 300 ms traveltime differential would require ~0.3 km/s average velocity change in the crust or alternately a crustal thickening of ~16 km. The same differential assigned to the lithosphere would require a change in lithospheric thickness of ~65 km. Clearly these are all large variations.

On the basis of the spatial variations observed, a full scale study should have a station spacing of ~100 km with several outlier stations also desirable; a 300 km by 300 km array of 16 stations is logistically manageable and would provide good data coverage. Based on this feasibility study, an 8 month observing period should provide a good basic data set for traveltime analysis. However for sufficient data redundancy, 12 months would be more appropriate. Unfortunately, due to the distribution of earthquake zones, certain azimuth and distance ranges will always be data deficient. A complete study must include examination of additional well logs to determine variability in the velocities of the sedimentary column and to include known basement velocities.

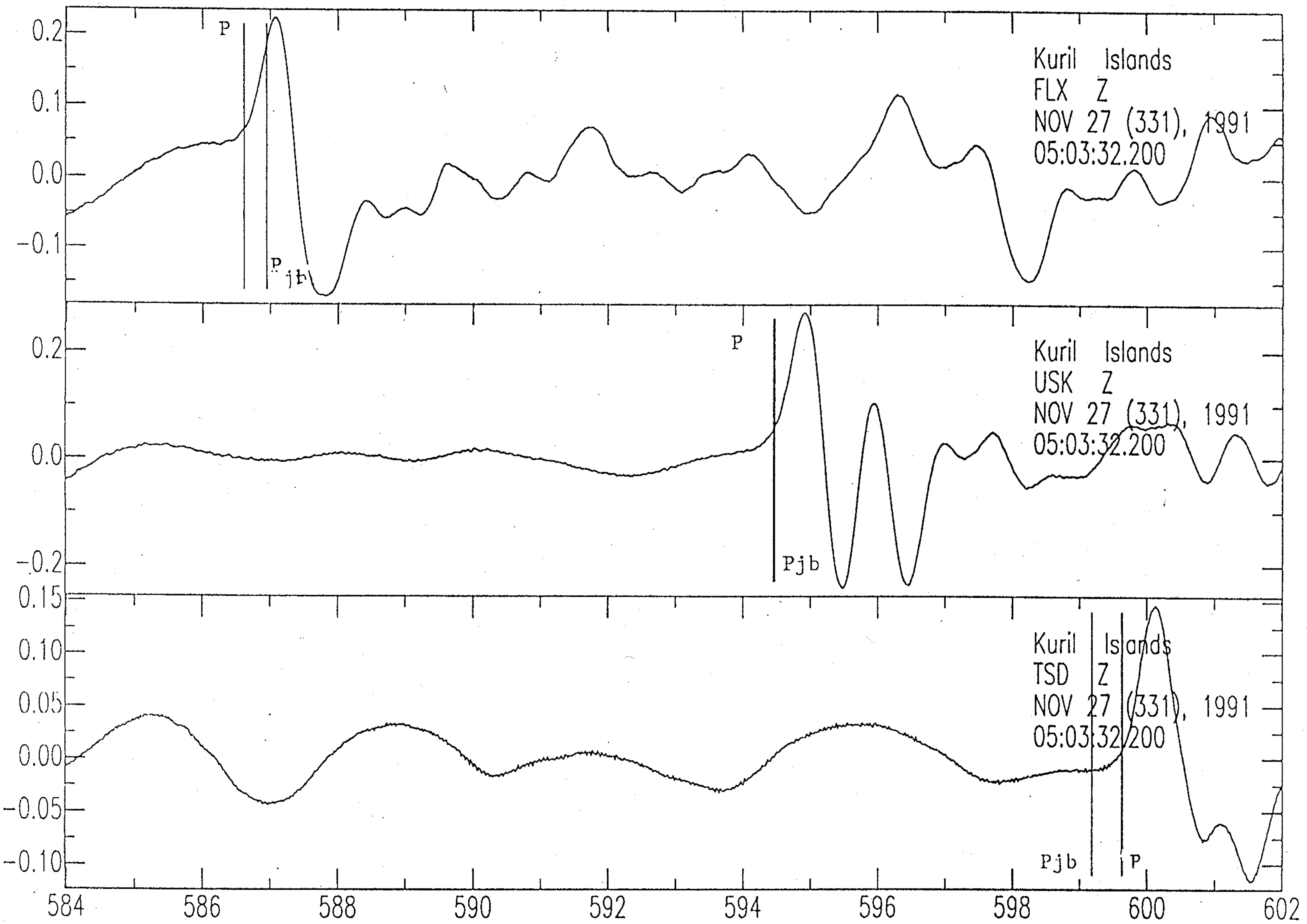

Figure 8a. Comparison of expected arrival times (Pjb) and picked arrival times (P) for an earthquake from the Kurile Islands (azimuth ~ 310⁰)

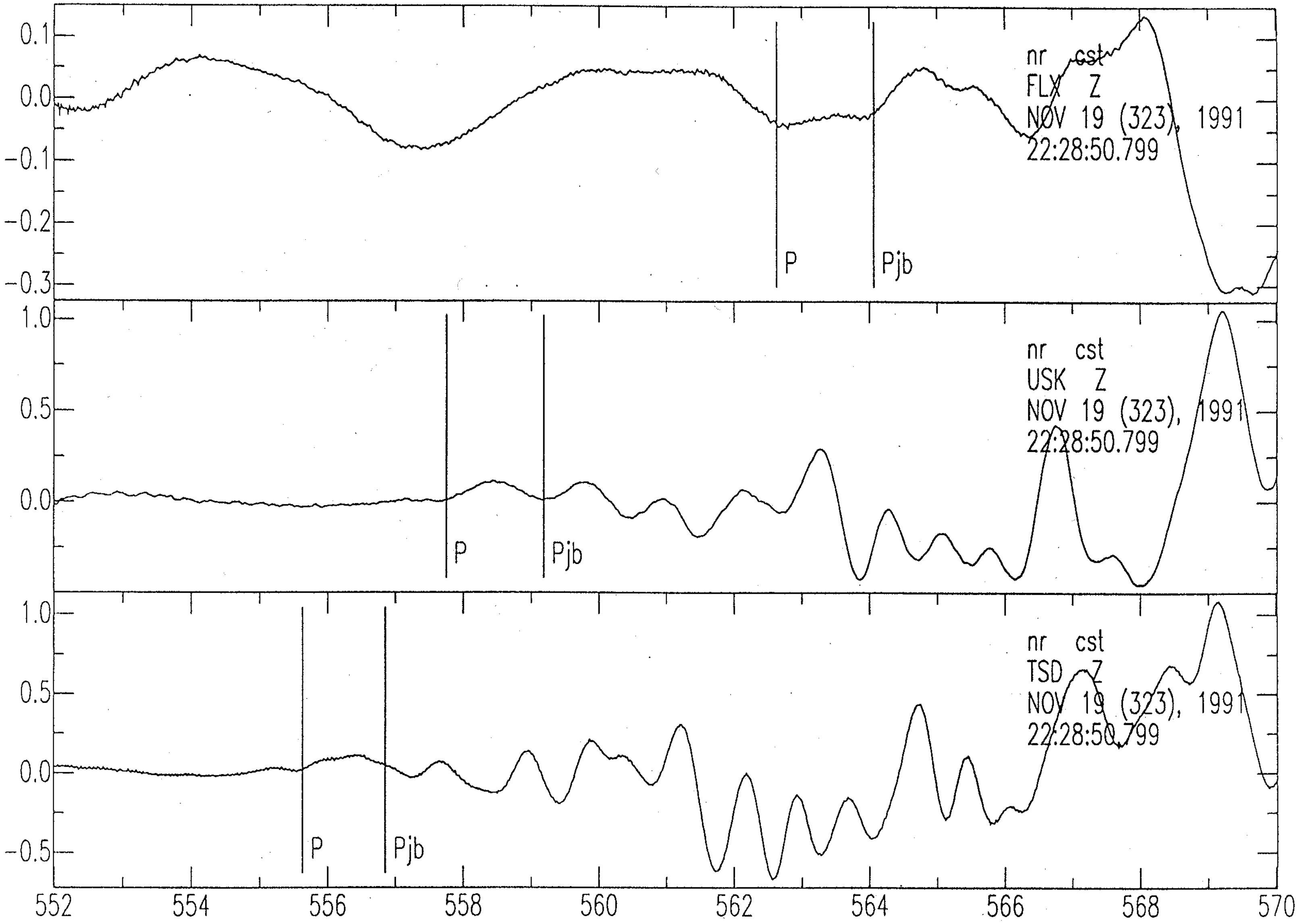

Figure 8b. Comparison of expected arrival times (Pjb) and picked arrival times (P) for an earthquake from the near the coast of Colombia (azimuth ~ 145⁰)

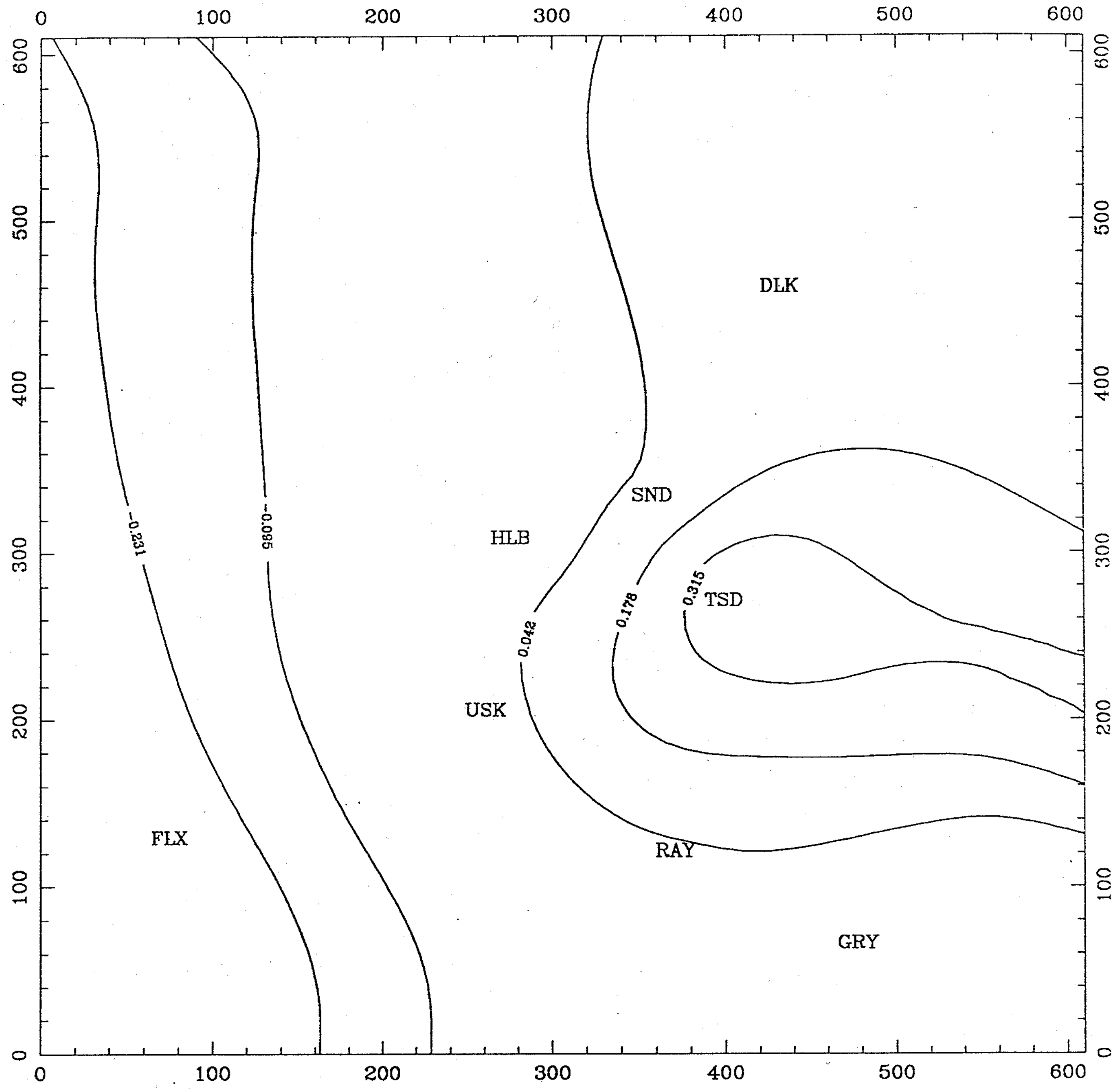

Figure 9a. Station residuals relative to USK for 15 earthquakes from Kurile Islands region (Δ ~ 62°, BAZ ~ 310°). Axes are distances in km.

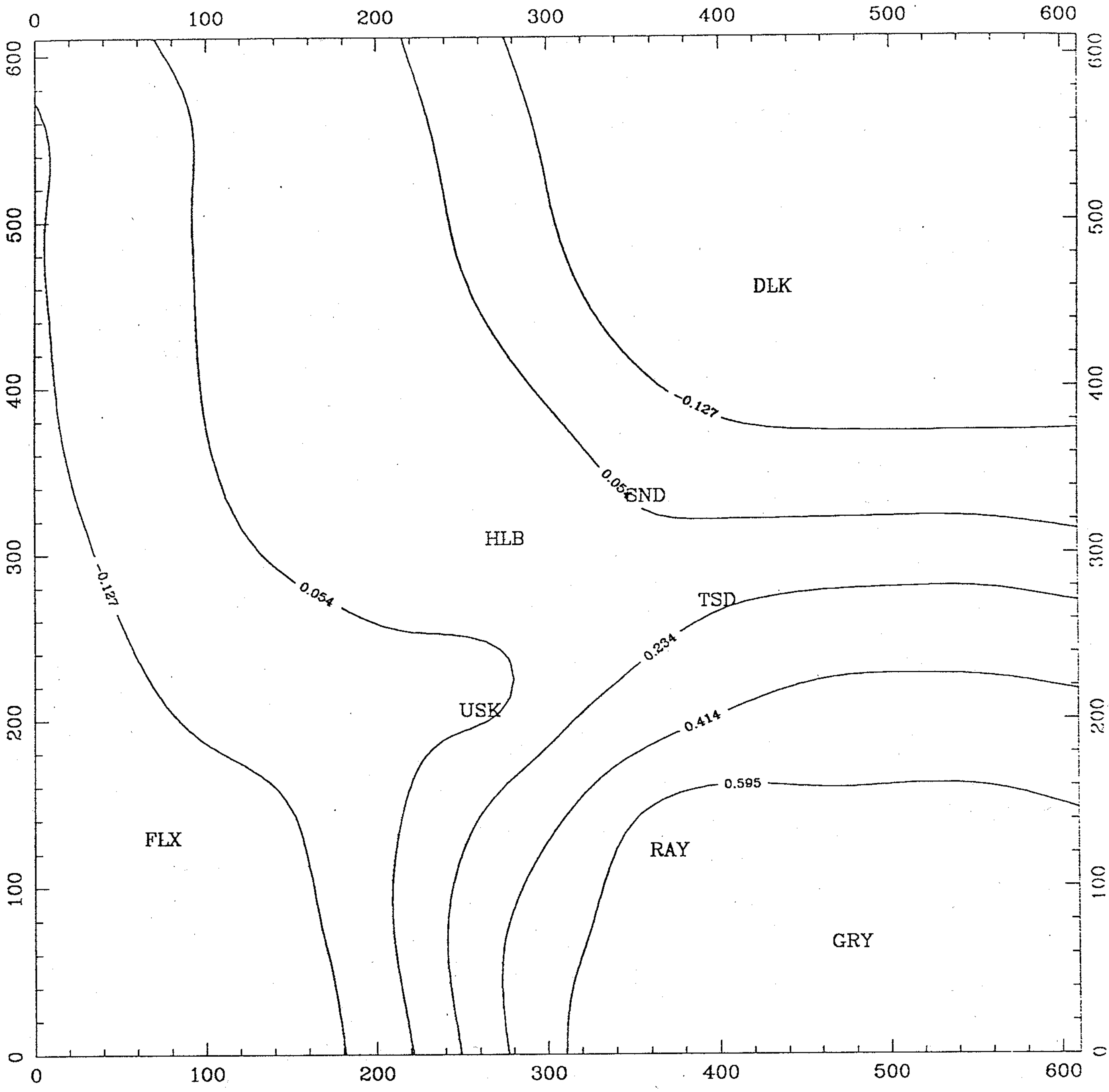

Figure 9b. Station residuals relative to USK for 9 earthquakes from coast of Colombia (Δ ~ 55⁰, BAZ ~ 147⁰).

TABLE 2

P-WAVE RESIDUALS

P-wave residuals (R) relative to station USK and associated standard deviations (σ). (Units are ms). Residuals are provided for two sets of earthquakes: (i) from Kurile Islands, and (ii) from coast of Colombia.

	$(\phi \sim 62^0, \Delta \sim 309^0)$		$(\phi \sim 55^0, \Delta \sim 147^0)$	
Station	R	σ	R	σ
DLK	76	24	-304	20
FLX	-296	48	-150	42
GRY	-16	70	728	80
HLB	-41	19	170	-
RAY	30	36	770	69
SND	88	56	18	25
TSD	451	73	213	103

Teleseismic Receiver Function Analysis

Time-domain receiver function analysis (Langston, 1979; Owens et al., 1984; Ammon et al., 1990) was developed to model the shear-wave converted phases and multiples recorded on the horizontal components of P waveforms. Early researchers utilized long-period WWSSN data to construct simple plane-layered models or models containing a few moderately dipping planar interfaces. Extension to higher frequencies introduced the need for more detailed models and a linearized time-domain inversion technique (Owens et al., 1984) for plane-layered modelling.

Method

In outlining the method, we follow the summary of Cassidy (1991). Mathematically, the vertical, radial and transverse ground displacement resulting from a plane P-wave impinging at the base of an earth model can be represented by:

$$D_Z(t) = S(t) * I(t) * E_Z(t) \qquad (1)$$

$$D_R(t) = S(t) * I(t) * E_R(t) \qquad (2)$$

$$D_T(t) = S(t) * I(t) * E_T(t) \qquad (3)$$

where $S(t)$ is the source time function, $I(t)$ is the instrument response (which is identical for all 3 components in this study), and $E_Z(t)$, $E_R(t)$ and $E_T(t)$ represent the impulse responses of the local earth structure and * is the convolution operator. The effective source function includes any arrival having a slowness value similar to that of the direct-wave (e.g. near-source and secondary phases such as pP and PcP).

Langston (1979) suggested that $E_Z(t)$ may be approximated as a Dirac delta function:

$$E_Z(t) \sim \delta(t) \qquad (4)$$

In practice, this assumption removes P-reverberations associated with horizontal interfaces from the radial receiver functions. This is not true for P-reverberations associated with dipping layers. Combining equations (1) and (4), it is apparent that the vertical component of ground motion is dominated by the parameters which need to be suppressed

$$D_Z(t) \sim S(t) * I(t) \qquad (5)$$

Therefore by combining equations (1) - (3) and (5), one can estimate radial and transverse receiver functions by deconvolving $D_Z(t)$ from the radial and transverse components of ground motion, respectively. The following derivation is for the radial receiver function. Transverse receiver functions are calculated in exactly the same way (substitute the subscript T for the subscript R). The deconvolution is performed in the frequency domain using spectral division:

$$E_R(\omega) = \frac{D_R(\omega)}{I(\omega)\, S(\omega)} \sim \frac{D_R(\omega)}{D_Z(\omega)} \qquad (6)$$

To stabilize this deconvolution the water-level method suggested by Helmberger and Wiggins (1971) is applied. This provides for a minimum allowable value for the denominator in equation (6). Finally a Gaussian spectral window, $G(\omega)$, is applied in the frequency domain to remove high frequency noise. Thus, in practice the deconvolution is

$$\tilde{E}_R(\omega) = \frac{D_R(\omega)\overline{D}_z(\omega)}{\phi(\omega)} G(\omega) \tag{7}$$

where $\tilde{E}_R(\omega)$ is the estimate of $E_R(\omega)$,

$$G(\omega) = e^{-\omega^2/4a^2} \tag{8}$$

and

$$\phi(\omega) = \max\left(D_z(\omega)\overline{D}_z(\omega),\ c \cdot \max\left[D_z(\omega)\overline{D}_z(\omega)\right]\right) \tag{9}$$

$\overline{D}_z(\omega)$ is the complex conjugate of $D_Z(\omega)$; ω is the angular frequency, c is the water-level parameter, expressed as a fraction of the maximum of the vertical power spectra, and 'a' controls the width of the Gaussian filter. Transformation back to the time domain provides the estimate of the receiver functions.

In the time domain, $\tilde{E}_R(t)$ may be thought of as the true (or ideal) receiver function (i.e. a spike series) convolved with an averaging, or blurring function. Thus, equation (7) may be written as

$$\tilde{E}_R(\omega) = \frac{D_R(\omega)}{D_z(\omega)} A(\omega) \tag{10}$$

where $A(\omega)$ is the averaging function given by

$$A(\omega) = \frac{D_z(\omega)\overline{D}_z(\omega)G(\omega)}{\phi(\omega)} \tag{11}$$

Absolute amplitudes of receiver functions are used in this study as suggested by Ammon (1991).

Synthetic receiver functions are obtained from synthetic seismograms, which are generated using a fast three-dimensional ray tracing scheme (Langston, 1977). The earth model is parameterized in terms of a series of constant velocity, planar, dipping layers over a half-space. For each layer in the model, P- and S-wave velocities, density, strike and dip angles, and thickness are specified. Synthetic vertical, radial and transverse seismograms are generated by specifying a back azimuth and ray parameter for the plane wave incident at the base of the model. A consecutive application of Snell's law in the local interface coordinate system allows rays to be traced to the receiver. Having determined path-lengths in each layer, the arrival time for each phase can be calculated. Amplitudes are calculated using wave potentials in the local coordinate system and applying the appropriate reflection or transmission coefficient at each interface. In addition to the direct arrival and conversions, the synthetic seismograms may include the free-surface multiples associated with each interface. This ray-tracer is best suited to horizontal or moderately dipping structure. Steeply dipping boundaries may intersect, resulting in geologically unrealistic earth models (Cassidy, 1991). Synthetic radial and transverse receiver functions are then generated by treating the synthetic seismograms in the same way as the real data. For the synthetic data we present, an 'a' value (Gaussian pulse width) of 5.0, corresponding to an upper frequency limit of ~1 Hz, was used.

Data

Based on preliminary inspection and analysis of the seismograms from the 5 broadband stations, 33 earthquakes yielding 98 three component station records appear suitable for analysis, i.e. an adequate signal-to-noise ratio and $\Delta > 30^0$. These are listed in Appendix D. As indicated in the appendix, there are an additional 54 station records, from these and an additional 22 earthquakes, of which a limited number of seismograms may be useful.

Processing and preliminary results

With respect to teleseismic deconvolution, there are three key questions which need to be answered in this feasibility study:

(i) In this experiment on the sediments (except for DLK), are there special problems, e.g will the strong conversions at the sedimentary-basement boundary mask all other effects and will special processing be required?

(ii) Can consistent Ps conversions be recognized?

(iii) How long must the recording period be?

To answer these questions, the seismograms at the 5 broadband stations (DLK, FLX, RAY, TSD, USK) were examined and a selected suite of records subjected to a preliminary analysis. No detailed interpretation was undertaken.

We first examined a suite of 4 earthquakes (225, 232, 249, 256) all of which have BAZ ~ 310^0 and $\Delta \sim 62^0$. These were processed individually and then stacked. In detail, numerous deconvolutions were performed to obtain receiver functions with the highest signal-to-noise ratio. However for most data, a water level parameter of 0.0001 and Gaussian width of a = 5, which removes high frequency noise (> 1 Hz), were used. Fig. 10 shows the results of the individual deconvolutions and the stacked results. Fig. 11 is a comparison of the stacks for the 5 broadband stations. Note that the noise before the P wave at 0 s provides a guide to the reliability of the apparent arrivals in the coda.

Although some of this data is rather noisy, strong event to event correlations are evident. For example at station DLK, there are clear peaks immediately following the first arrival and a very strong arrival at ~4.8 s; on FLX, there are a series of strong positive arrivals culminating with a very large one at 5 s and then a negative at ~7 s; RAY is characterized by a double peak onset, a strong negative in the 1.5 - 2.5 s range, and a complex series of arrivals in the 3.5 - 5 s range; USK has a negative at ~5 s and a consistent pattern in the 10 - 12 s range. We note that arrivals in the 5 s range correspond to depths of ~45 km; the consistent arrivals from beyond 10 s for USK correspond to depths well into the upper mantle. At TSD, only in the first 2 s is the signal-to-noise ratio adequate. At the stations other than TSD, clear correlations exist in the first 2.5 s. Further, there are distinct arrivals, albeit at slightly different times, near 5 s and in the 10 - 12 s range. Thus, there is evidence that clear conversions exist at Moho and deeper levels which we can anticipate will be interpretable as they are consistent in the convolutions at the stations and are correlate between sites.

In a further examination of the data, we compare the deconvolutions of the previous suite of earthquakes with those using a suite of 3 earthquakes (80, 153, 198) from the same azimuth but a slightly greater distance, i.e. 68^0 compared to 62^0. For interpretable structure, the expected differences between deconvolutions is a slight shift in the peaks and troughs due to the different traveltimes resulting from the change in angle of incidence. The comparison is shown in Fig. 12; note the horizontal scale change from Fig. 10 and 11. For DLK, a convolution which does not show strong later arrivals, the only readily correlatable phases are near 2 s and possibly in the 12.5 - 15 s range. At the other stations very clear correlations exist over the first 10 s. It is particularly interesting to note that the arrival beyond 10 s persists at USK.

The final test we performed was to compute the theoretical deconvolution at each station for a model which contained the sediment thickness as a single layer and its known average velocity (Table 4) for comparison with the observed deconvolutions for the suite of earthquakes from BAZ ~ 310^0 and $\Delta \sim 62^0$ (Fig. 13). While the arrivals generally correlate, the theoretical deconvolutions contain much larger reverberations than those observed; note that there are no sediments at DLK. The current ray tracing algorithm used in the processing sequence uses $Q = \infty$, a clearly inappropriate value for the sediments. From this calculation, it is evident that most of the character in the first ~2.5 s is due to the basement-sediment interface. Beyond this time, other arrivals are

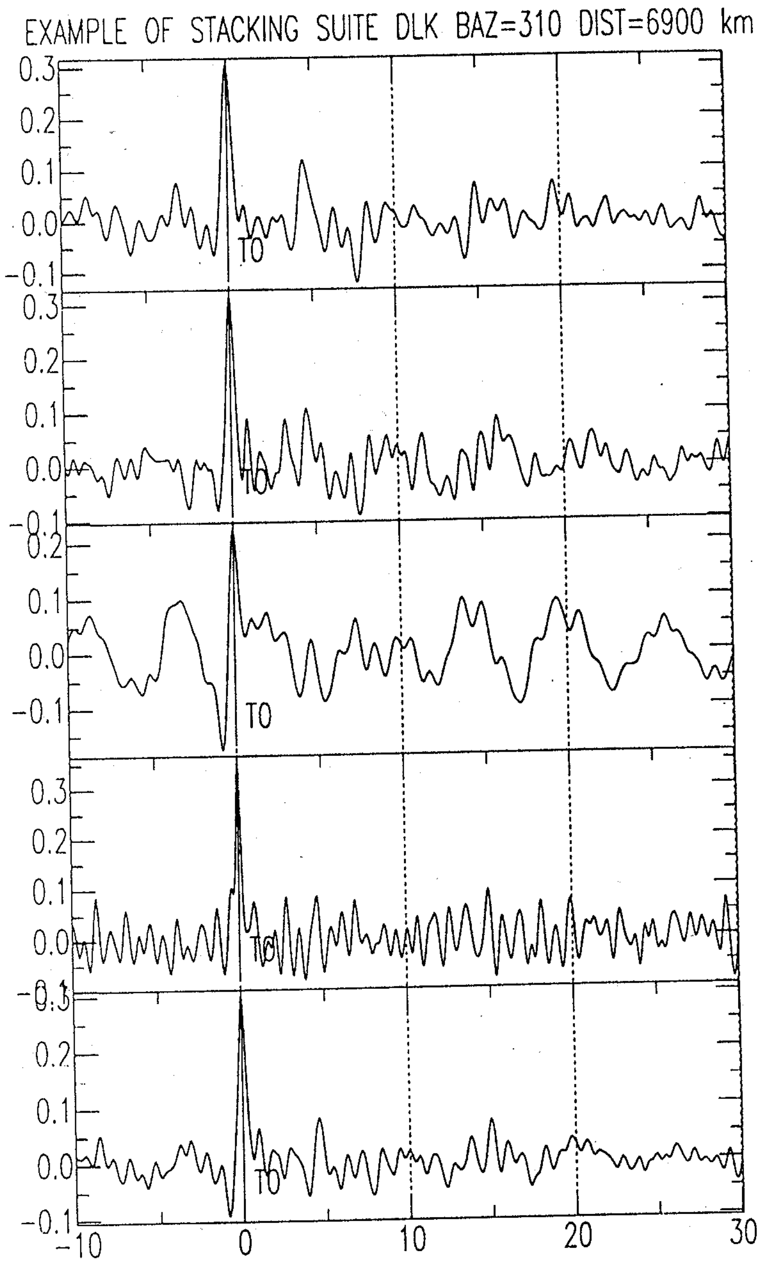

Figure 10a. Four radial receiver functions for DLK and the stacked result (lower trace). For all plots of receiver functions horizontal axis is time (s).

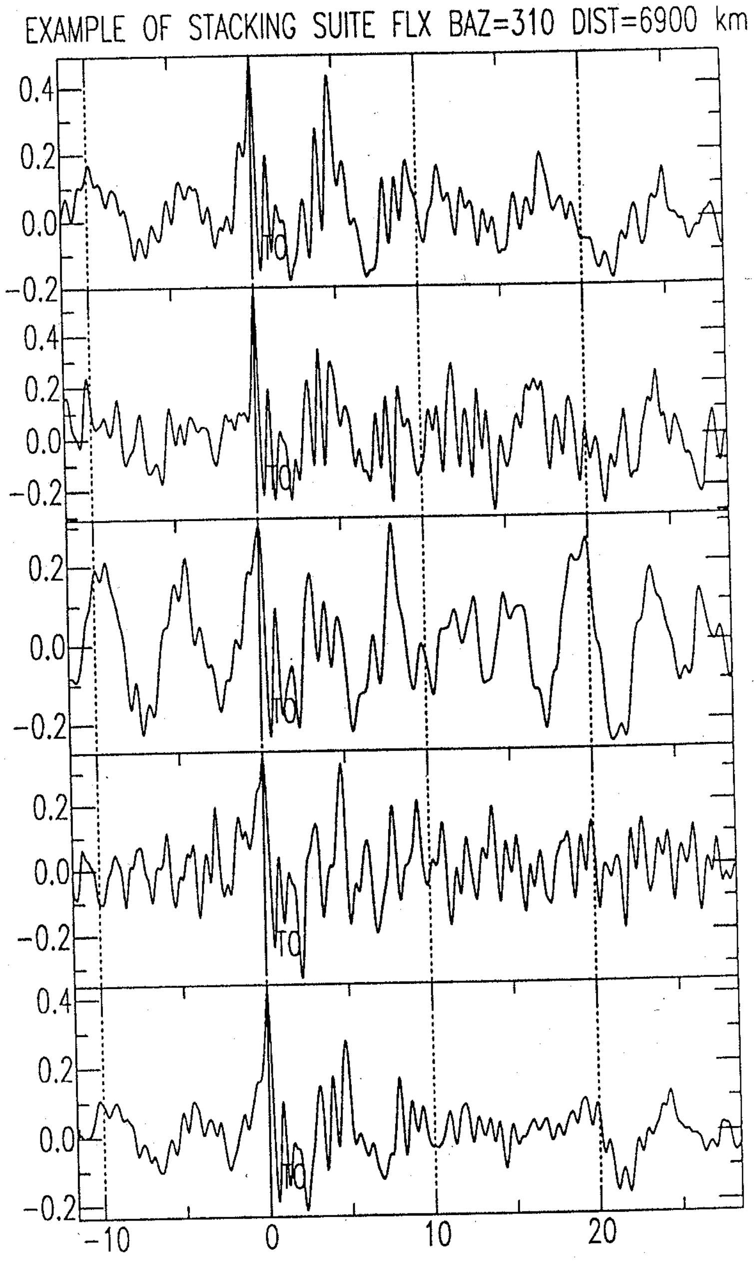

Figure 10b. Four radial receiver functions for FLX and the stacked result (lower trace).

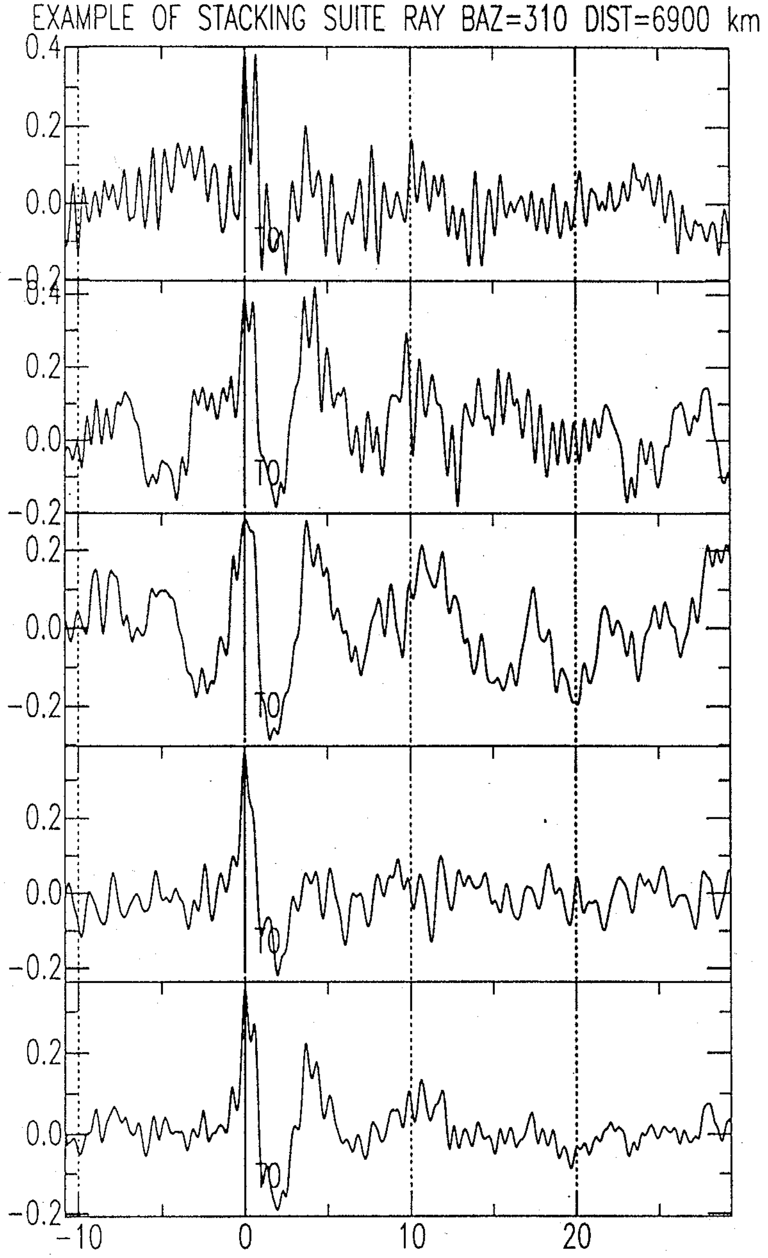

Figure 10c. Four radial receiver functions for RAY and the stacked result (lower trace).

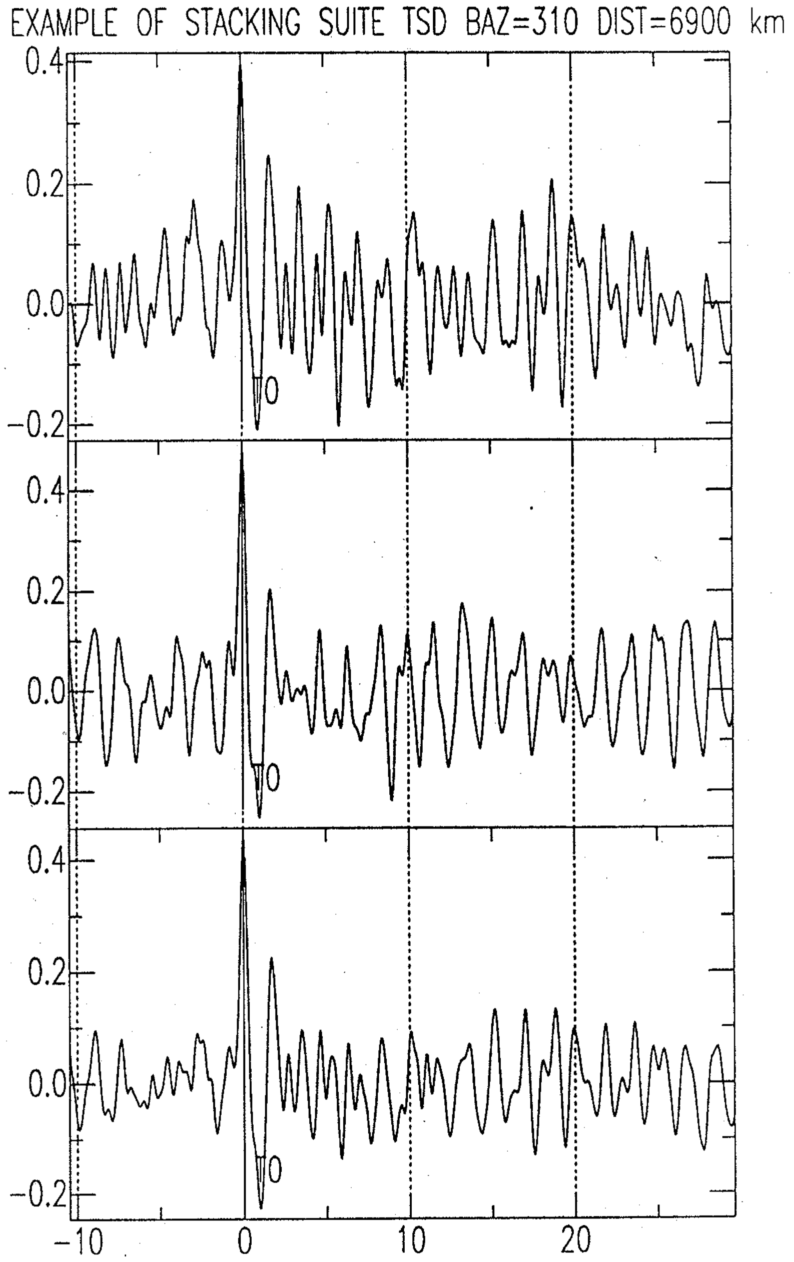

Figure 10d. Two noisy radial receiver functions for TSD and the stacked result (lower trace).

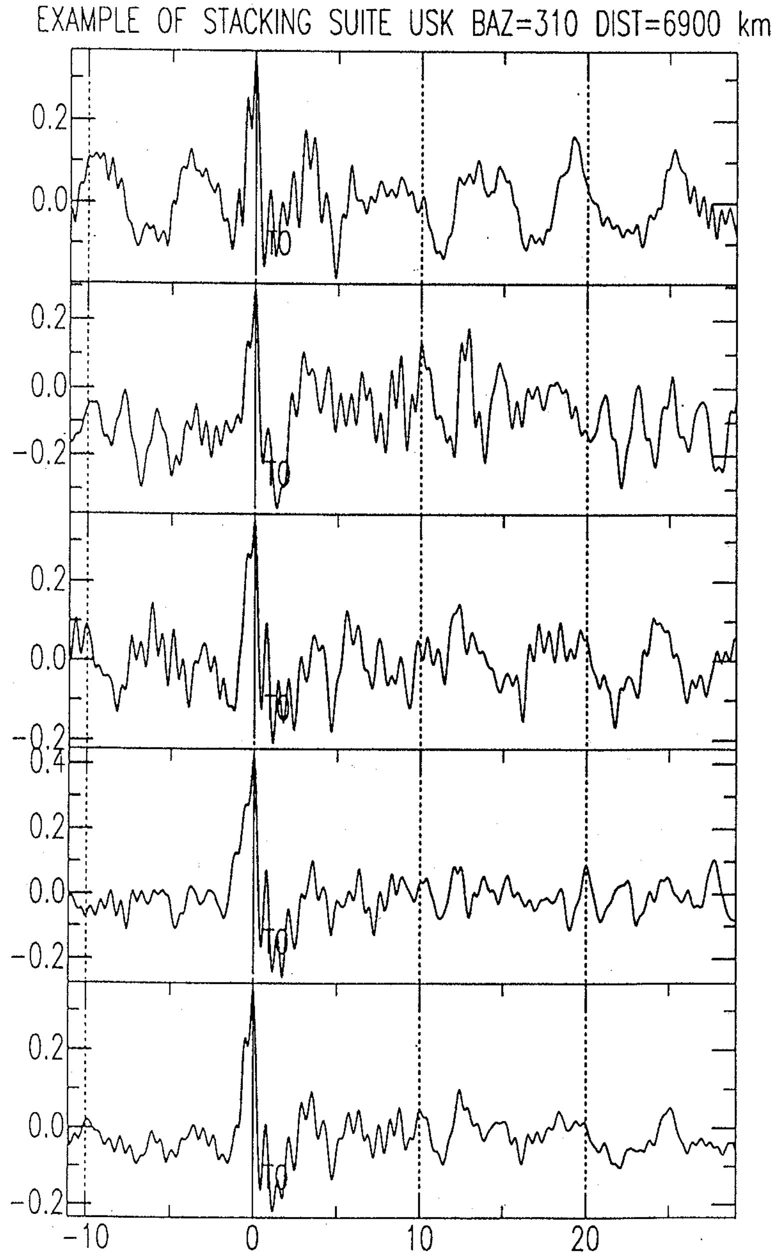

Figure 10c. Four radial receiver functions for USK and the stacked result (lower trace).

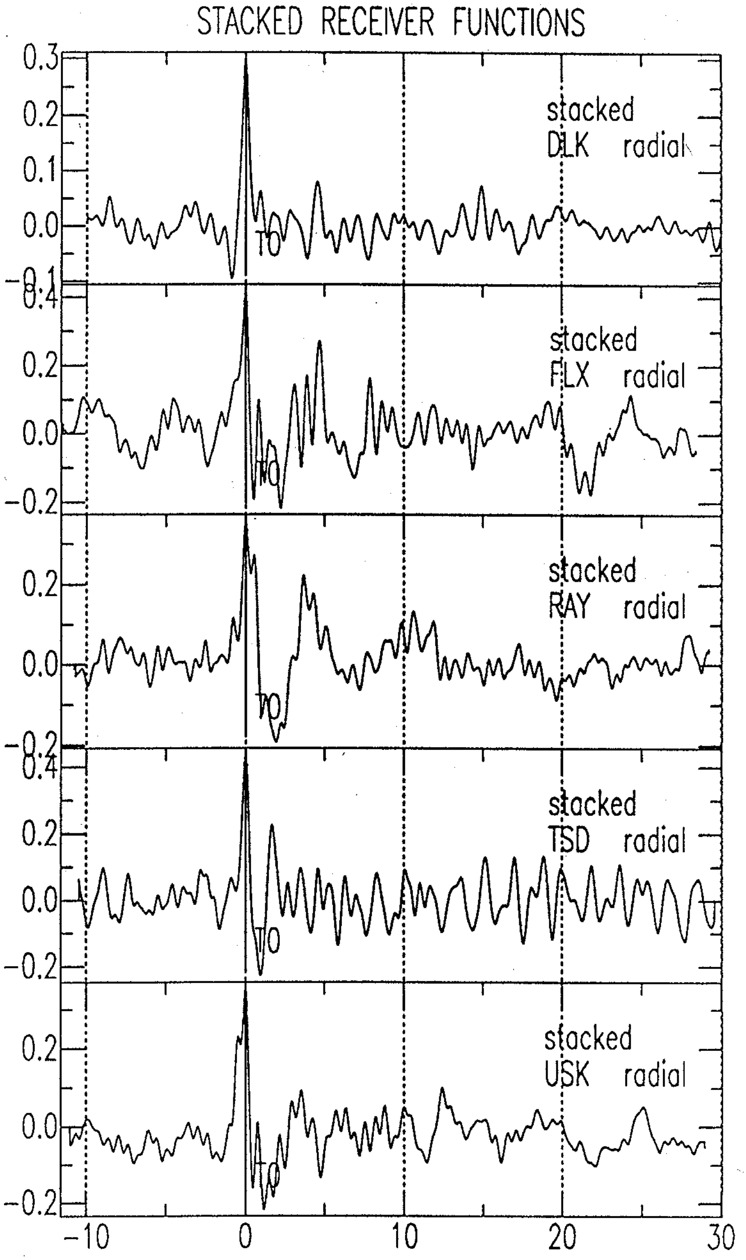

Figure 11. The stacked receiver functions for the 5 broadband stations.

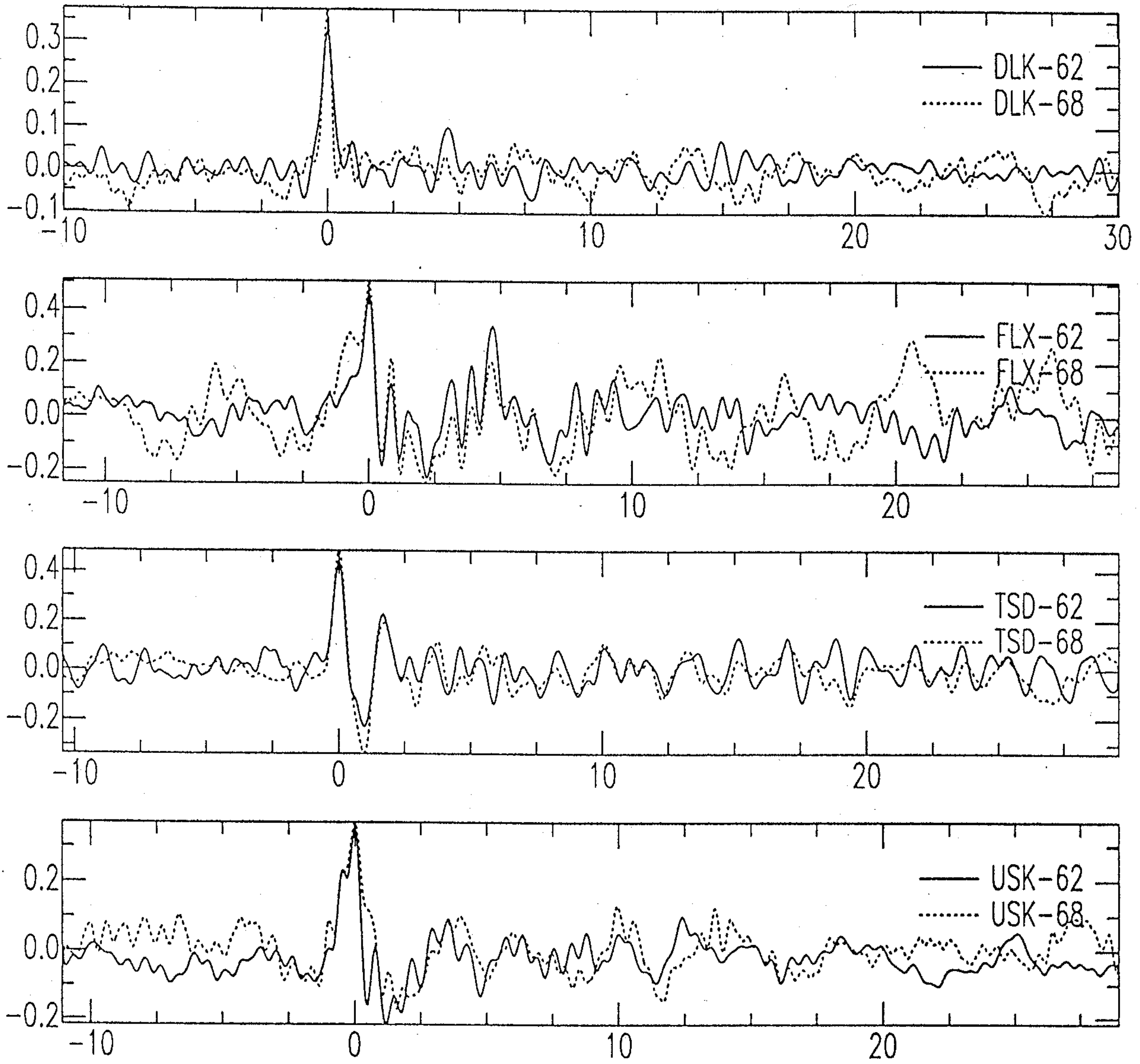

Figure 12. Comparison of two stacked radial receiver functions at stations **DLK, FLX, TSD** and **USK**. Seismograms in both stacks are at BAZ = 310° but slightly different Δ's (62° and 68°).

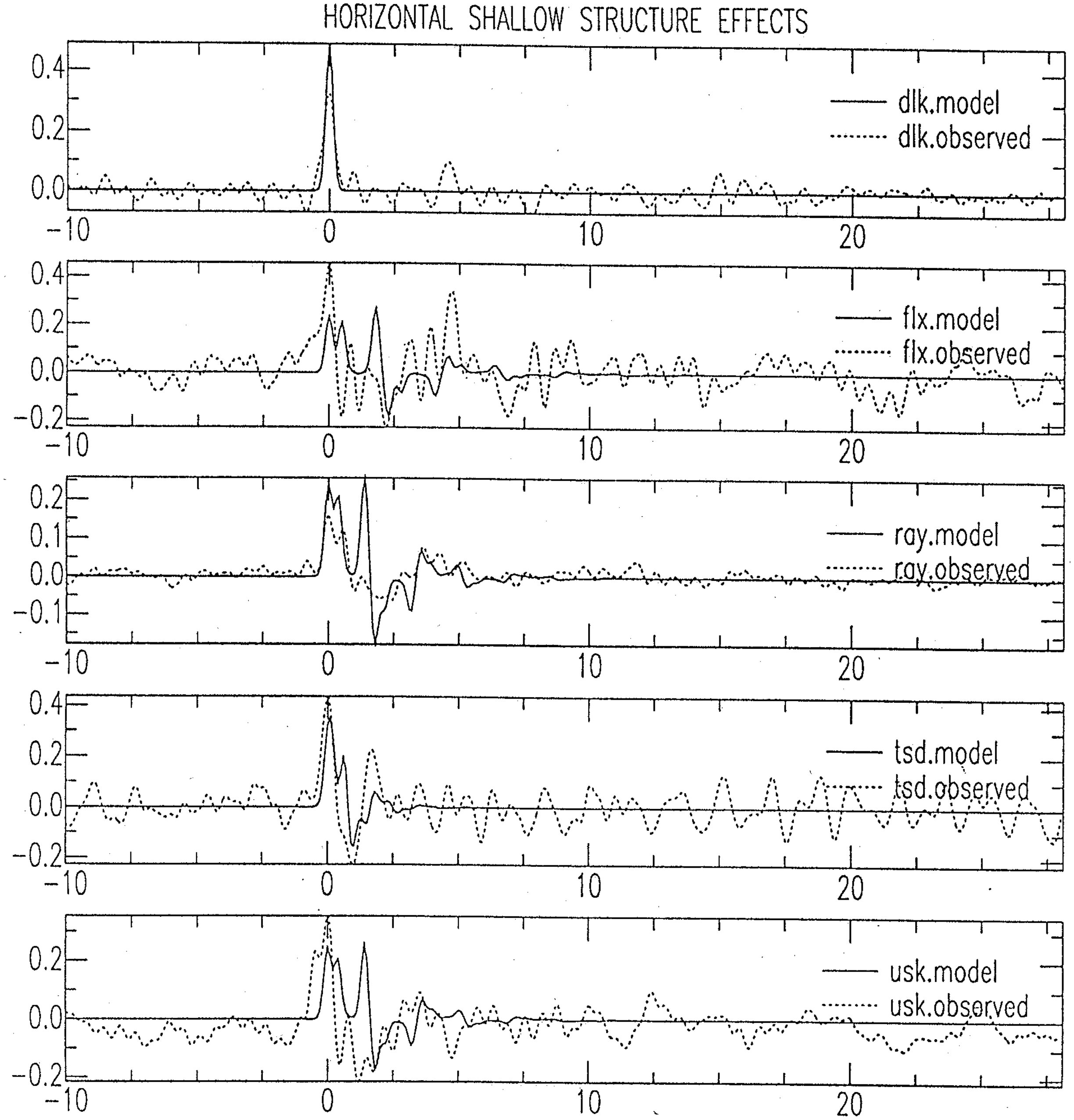

Figure 13. Comparison between observed and theoretical radial receiver functions at broadband stations ($\Delta \sim 62^0$, BAZ ~ 310^0). The theoretical models contain only a single layer sedimentary section based on well logs and the basement (Table 4). Q is infinite.

Table 4:

Reference model used for shallow structure modeling (where: V_P is $P-$wave velocity in km/sec; V_S is $S-$wave velocity in km/sec; ρ is density in g/cm^3; Th is layer thickness in km; σ is Poisson's ratio).

Station	**DLK**						
Layer No.	V_P km/s	V_S km/s	ρ g/cm^3	Th km	strike	dip	σ
1	6.50	3.75	2.85	∞	0.00	0.00	0.25
Station	**FLX**						
1	3.32	1.92	1.83	2.15	0.00	0.00	0.25
2	6.00	3.46	2.69	∞	0.00	0.00	0.25
Station	**RAY**						
1	3.35	1.93	1.84	1.72	0.00	0.00	0.25
2	6.00	3.46	2.69	∞	0.00	0.00	0.25
Station	**TSD**						
1	3.54	2.04	1.90	0.88	0.00	0.00	0.25
2	6.00	3.46	2.69	∞	0.00	0.00	0.25
Station	**USK**						
1	3.39	1.96	1.86	1.78	0.00	0.00	0.25
2	6.00	3.46	2.69	∞	0.00	0.00	0.25

the key contributors. Thus, we conclude that a ray tracing algorithm which allows finite Q should be used and there are clear arrivals which cannot be explained by the sedimentary section.

Recording period: Owens et al. (1987) have found that events below body wave magnitude of about 5.7 are rarely useful for waveform analysis unless they occur at distances less than 50^0. In a one year field program, they acquired 59 earthquakes suitable for analysis. Similarly, Cassidy (1991) in a two year period recorded 117 earthquakes. Stations FLX, TSD and USK operated for 6 months during which time 33 suitable earthquakes were recorded. Thus, our capture rate was effectively the same as these other workers, albeit in a different geological environment. They agree (Cassidy, personal communication) that at this capture rate a minimum of one year's data is required, 18 months is preferable particularly if the structure is complicated. Only if one is successful in obtaining several superior records and the structure is simple should the experiment be of shorter duration.

Summary Comments

Examination of records and tests on the data lead to the following conclusions:

(i) For stations on the thick sediments, the effects of the sediments dominate the first 2.5 s of the receiver functions.

(ii) For modelling at stations located on the sediments, a ray tracing algorithm which allows finite Q should be used.

(iii) Clear arrivals are consistently present in the receiver functions from Moho depths and into the upper mantle. Comparison of individual receiver functions at stations and stacked receiver functions between stations suggests that physical parameters can be extracted at both crustal and upper mantle depths.

(iv) A minimum of one year's data should be acquired for a complete analysis.

SKS Anisotropy

Physical Basis for Measurements

The seismic phase SKS travels through the mantle as a shear wave, through the outer core as a compressional wave and travels upward at a very steep angle to the receiver again as a shear wave (Fig. 14). Due to the conversion from a P wave to an S wave at the core-mantle boundary, it will be polarized in the vertical plane of propagation for a spherically symmetric and isotropic Earth, i.e. the transverse component of energy, SKS_T, will be identically zero. Both anisotropy and aspherical structure can produce a non-zero SKS_T through shear-wave splitting and perturbations to the ray path respectively. These two possibilities can be distinguished on the basis of particle motion analysis. For aspherical structure, the particle motion will remain predominantly rectilinear, whereas for shear-wave splitting the particle motion will be elliptical (Silver and Chan, 1988).

Three hypotheses have been put forward to explain the observed anisotropy. However, in each case the shear-wave splitting depends on the same basic phenomena, i.e. alignment of the mantle minerals. Silver and Chan (1991) consider three possible processes:

(i) Absolute plate motion - this mechanism would be similar to what is believed to occur in the oceanic upper mantle with strain being concentrated in the asthenosphere but possibly producing strain in the lithosphere as well;

(ii) Present -day stress - assumes that the stress measured in the continental crust reflects lithospheric-wide stress that ultimately produces strain-induced anisotropy;

(iii) Internal coherent deformation - here the postulate is that the mantle isotropy is dominated by the last significant episode of internal coherent deformation.

They argue that the last hypothesis is the most successful.

Measurement of Shear-Wave Splitting Parameters

In the case of SKS, which propagates almost vertically, and assuming transverse isotropy, the radial and transverse components $u_r(t)$ and $u_t(t)$, are simply related by:

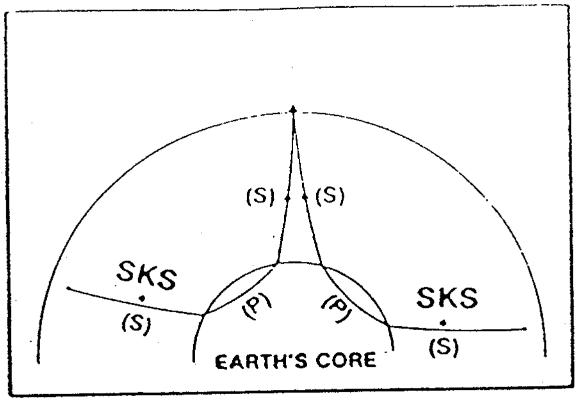

Figure 14. Path of the SKS phase from source to receiver (from Silver and Chan (1988).

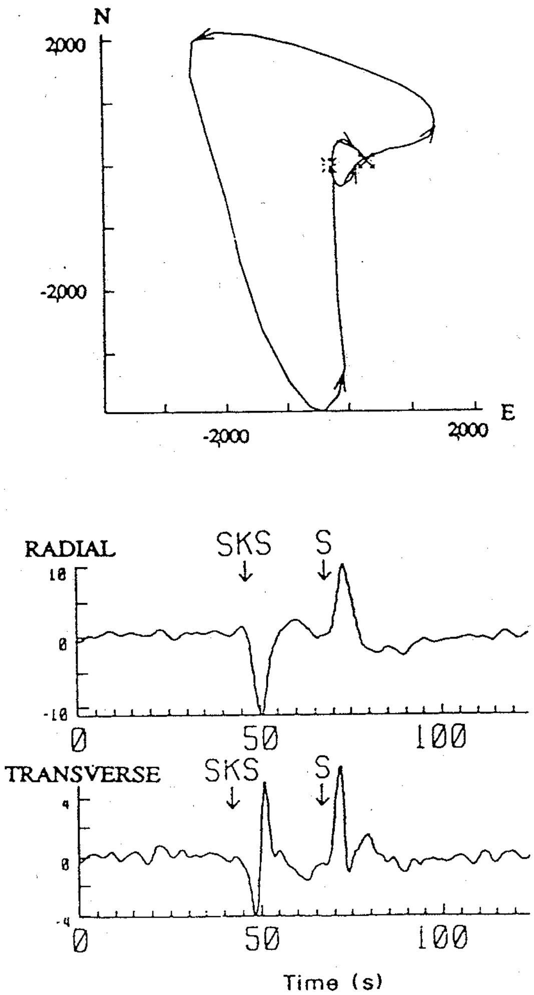

Figure 15. Radial and transverse SKS seismograms (lower); note that the transverse component is non-zero and approximately the time derivative of the radial component. In the upper diagram, the elliptical horizontal partical motion is shown (from Siver and Chan. 1988).

$$u_r(t) = s(t) \cos^2 \phi + s(t - \delta t) \sin^2 \phi \qquad (12)$$

$$u_t(t) = -0.5[s(t) - s(t - \delta t)] \sin (2\phi) \qquad (13)$$

where s(t) is the radial waveform in the absence of anisotropy and ϕ is the angle between the fast and radial directions. For small δt compared to the dominant period of s(t), the change in radial component will be subtle, a slight broadening and distortion. In contrast, the transverse component will be approximately proportional to the time derivative of the radial component [equation (13)]. Silver and Chan (1988, 1991) have shown that in certain cases that SKS_T is clearly observed, about the same amplitude as SKS_R, and that elliptical rather than rectilinear particle motion is present. An example of observed radial and transverse components and the resultant horizontal particle motion are shown in Fig.15. They infer that the transverse-component signals are predominantly caused by azimuthal anisotropy. Absence of SKS_T in the presence of a strong SKS_R will of course occur if the back azimuth is along the fast or slow polarization direction (see equation 13).

To measure the shear-wave splitting parameters, we use one of the techniques used by Silver and Chan (1988, 1991) suggested by Bowman and Ando (1987), i.e. we search for the pair ϕ and δt that, when used to correct for the anisotropy, most successfully removes its effect. Because SKS is initially radially polarized, this may be simply done by minimizing the energy $E_t(\phi,\delta t)$ on the reconstructed $\tilde{u}$ (t) transverse component u(t) of the N-point digital time series:

$$E_t(\phi,\delta t) = T^{-1} \int_0^T \tilde{u}_t(t)^2 \, dt \sim N^{-1} \sum_{n=1}^{N} (\tilde{u}_t^n)^2 \Delta t \qquad (14)$$

E_t may be quickly evaluated for many candidate values of ϕ and δt (increments of 1^0 and 0.05 s, respectively) as it can be expressed as a linear combination of the auto- and cross-correlations of the original E-W and N-S seismograms (Silver and Chan, 1988).

SKS data

The best distance range for splitting measurements is 85^0 - 110^0, where SKS is both well isolated from S and ScS ($> 85^0$) and sufficiently energetic ($< 110^0$). Optimally, deep events should be used as the waveforms are simpler and will not be attenuated by two passages through the asthenosphere. In the current investigation, the two earthquakes shown in Fig.16 and 17 clearly recorded the SKS phase in the seismic wave train. Event 166 (Fig. 16) shows a clear SKS phase w on the N component but with S/N of <2; it is not observable on the E component. Therefore no analysis was performed. Event 156 (h = 193 km, $\Delta \sim 86^0$, M = 5.8, BAZ = 295^0) shown in Fig. 17 exhibits our best recorded SKS phase. Unambiguous ground motion is observed on both horizontal components.

SKS Results

Our data processing was done following method of Silver and Chan (1988, 1991) and is demonstrated on Fig. 18 and 19 using Event 156 shown in Fig. 17. First, the horizontal N and E components are rotated into the radial and transverse directions (upper two panels of Fig. 18). (Note: for the purposes of this display, radial is defined as BAZ - 180^0 and transverse as Radial + 90^0.) We note that a small amplitude SKS_T is present. The records are then processed as indicated above to obtain the fast direction of 125^0 and time delay of $\delta t = 0.27$ s. The bottom two panels shows the reconstructed radial and transverse phases. On the reconstructed seismograms, the SKS_T phase is no longer evident as is expected.

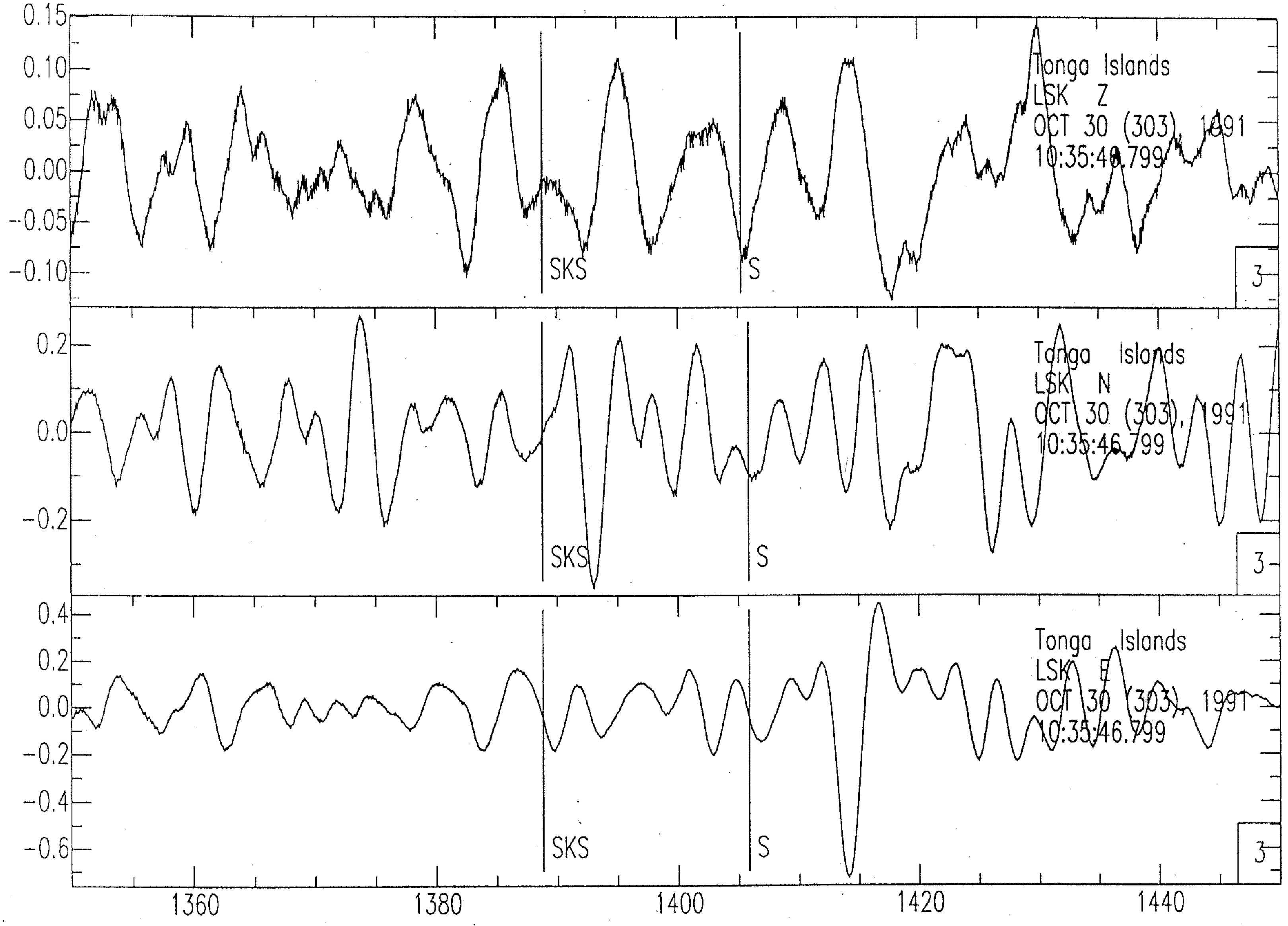

Figure 16. Seismograms from a Tonga Islands earthquake showing an SKS phase on the N component The low S/N renders this event unusable.

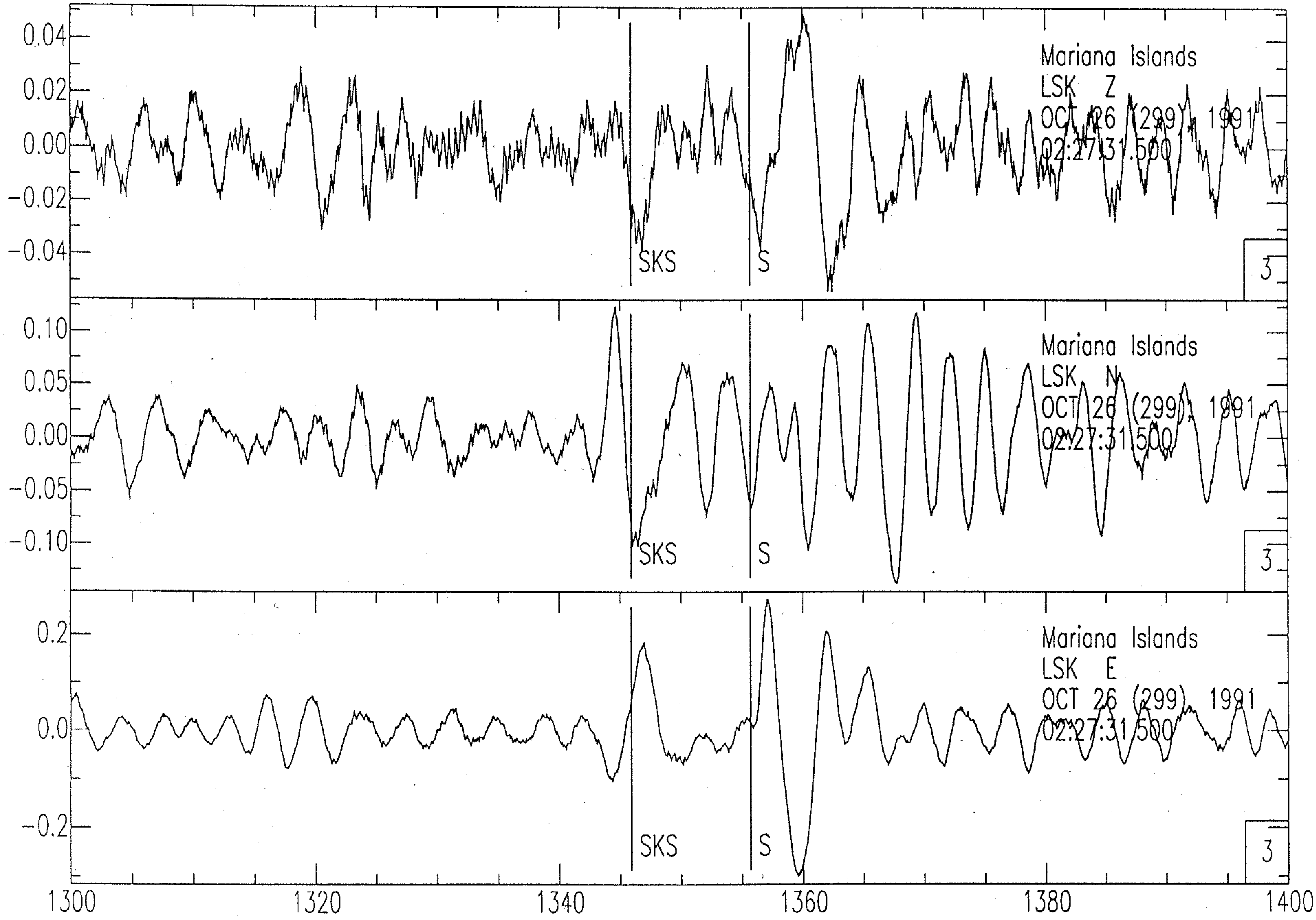

Figure 17. Seismograms from a Mariana Islands earthquake (Event 156) showing well-recorded SKS phase on both the N and E seismograms. Processed records for this event are shown in Fig. 18 and 19.

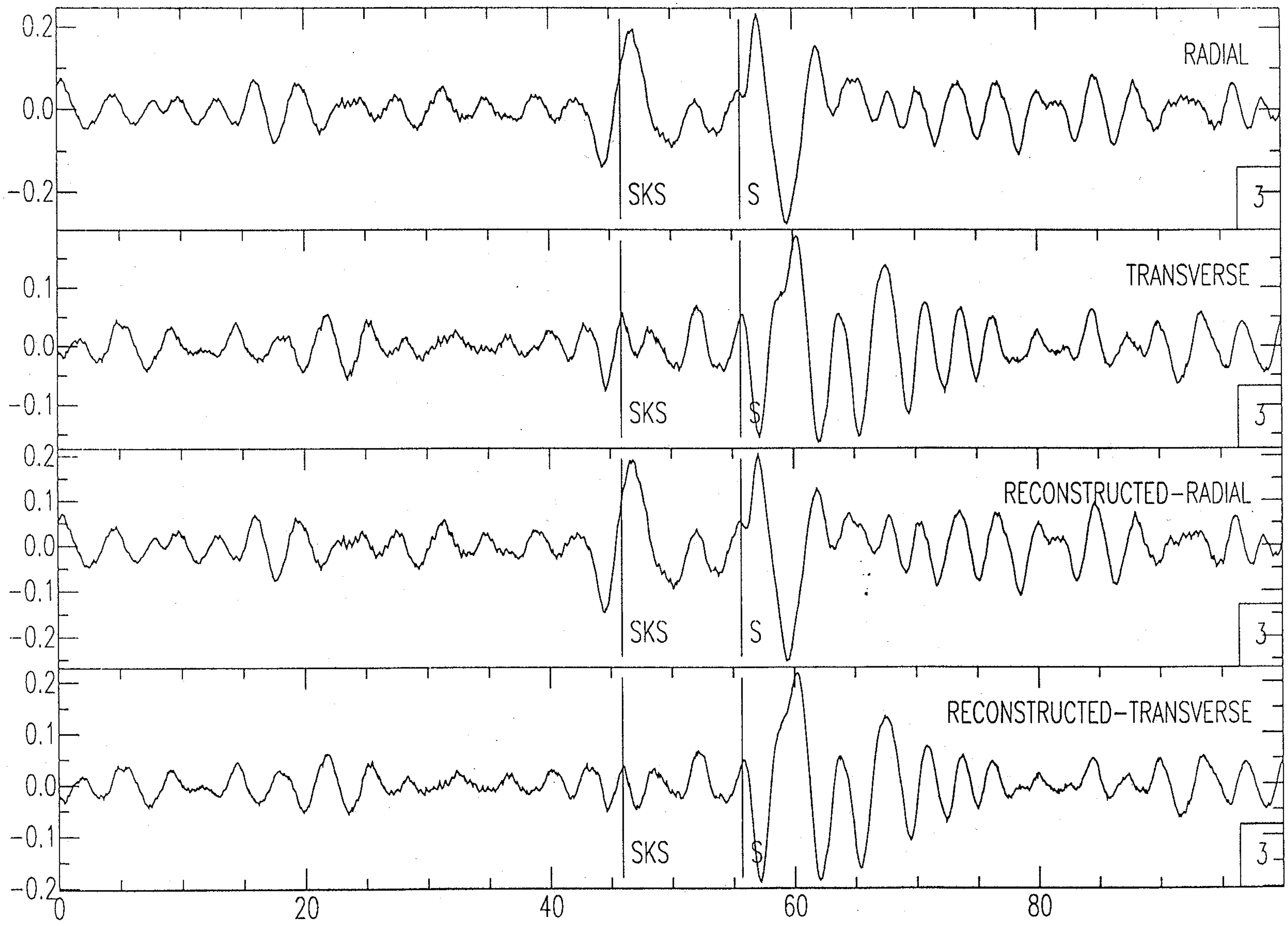

Figure 18. The upper two panels show radial and transverse components of of Event 156. The lower two panels shows the reconstructed radial and transverse. In this case the transverse energy in the SKS phase is no longer evident.

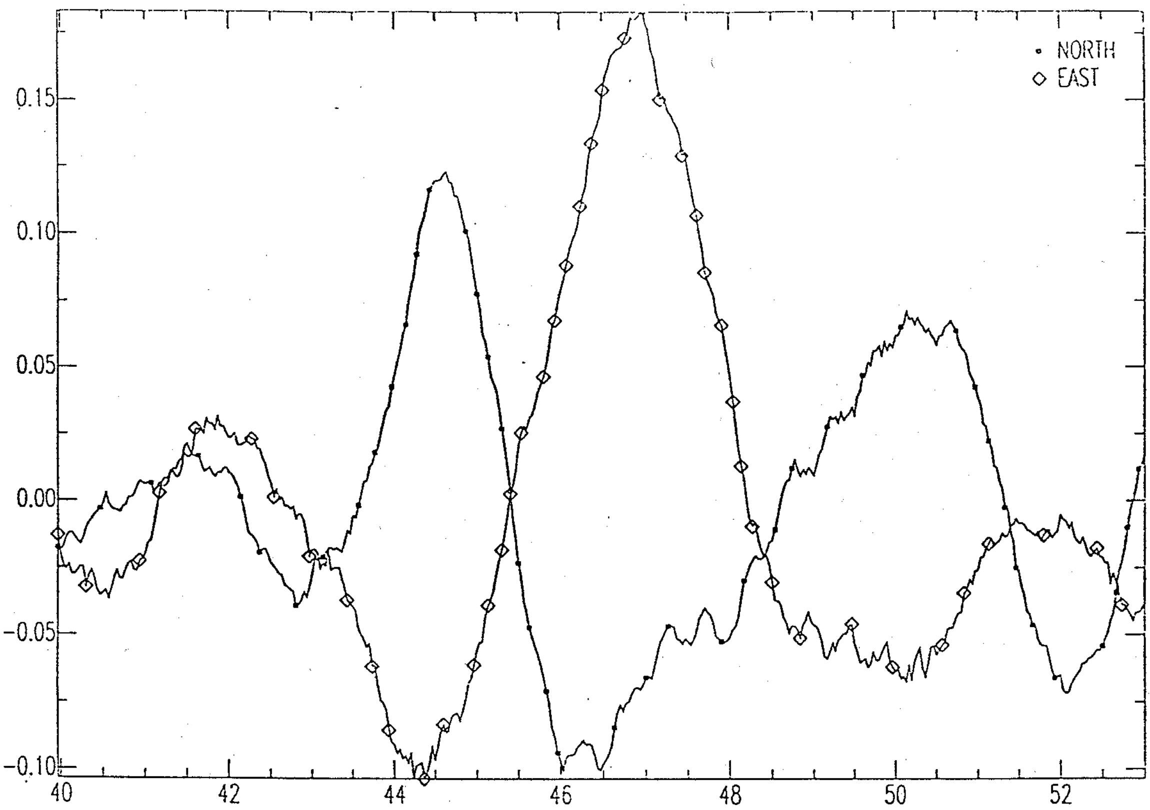

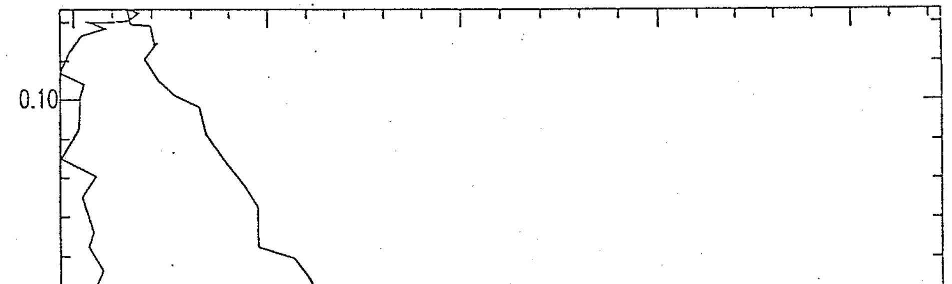

Figure 19a. Upper: uncorrected horizontal ground motion for Event 156.
Lower: horizontal particle motion as observed.

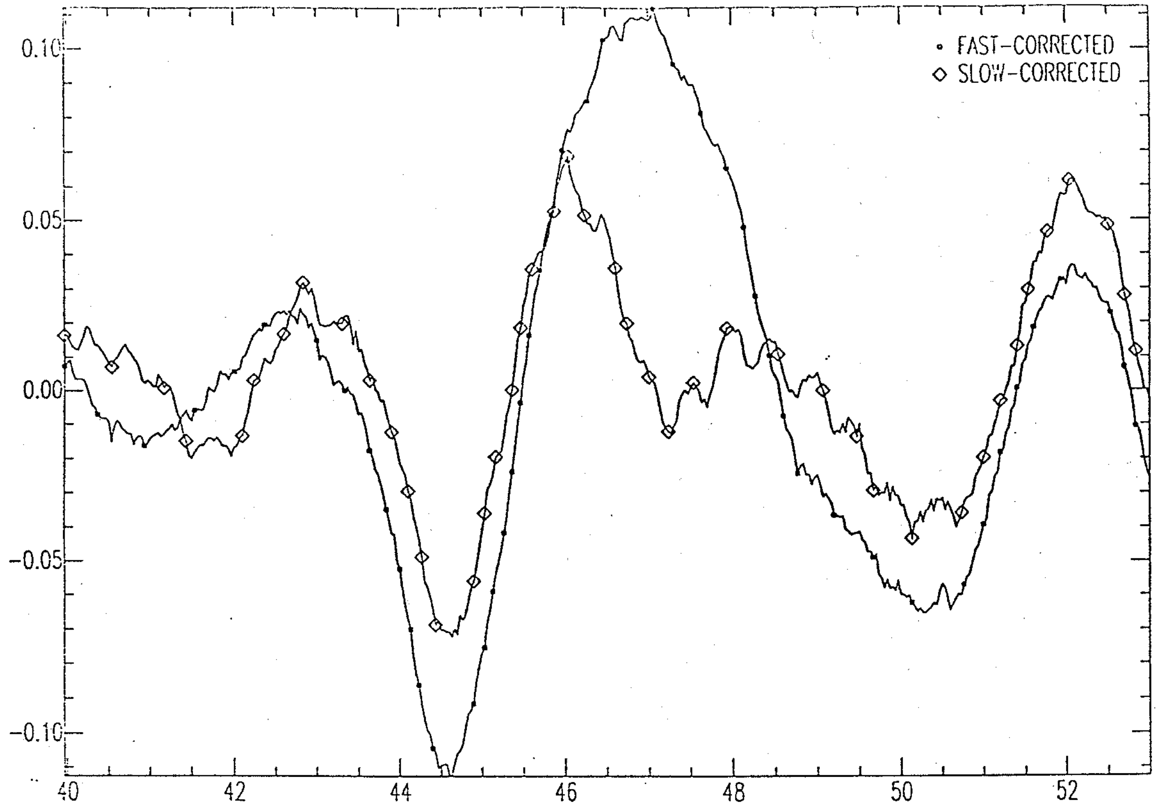

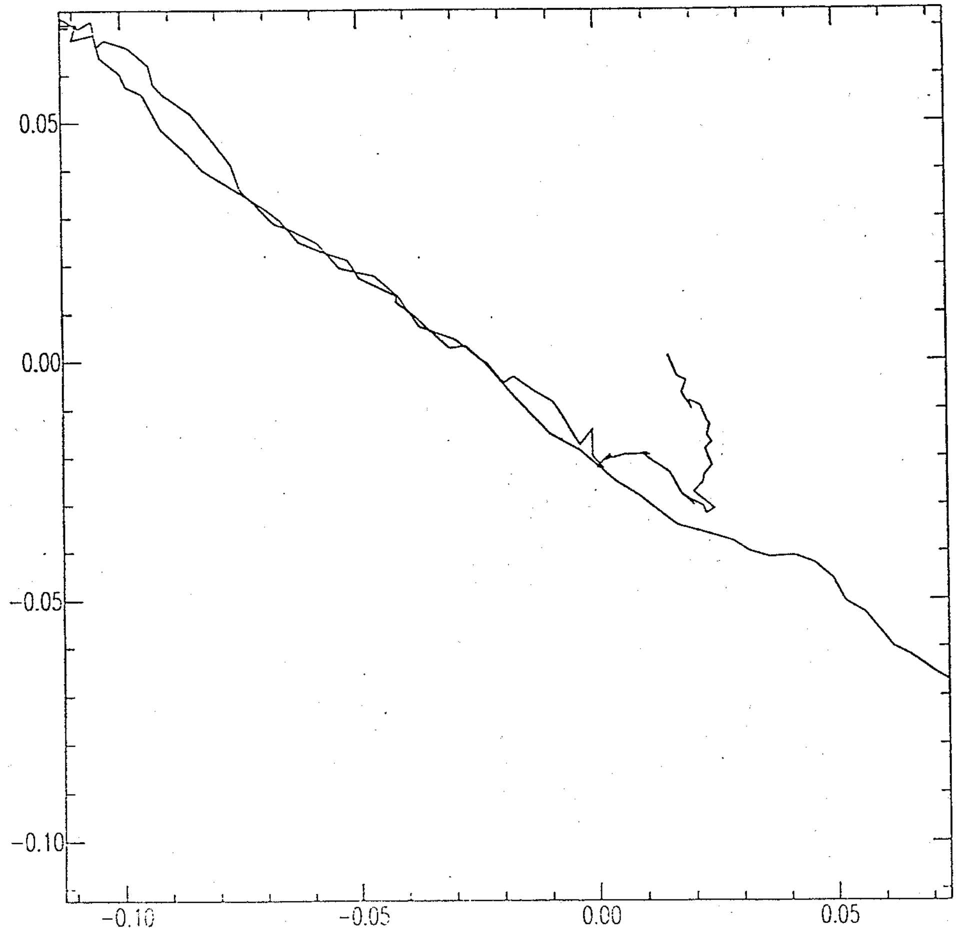

Figure 19b. Upper: Particle motion for Event 156 after correction.
Lower: Linear particle motion after 0.27 s shift.

Fig. 19a shows the SKS section of the seismogram and the uncorrected ground motion exhibiting elliptical polarization. Fig. 19b shows the corresponding corrected components and the ground motion after the 0.27 s shift between transverse and radial. Now the motion is rectilinear as it should be.

Comments on SKS Experiment

(i) The only earthquake analyzed (Event 156) is indicative of anisotropy with a fast direction $\phi = 125^0$ and delay $\delta t = 0.27$ s. We note that the S/N is not high and therefore these parameters should be treated with great caution. By comparison the well-recorded events (see for example Fig. 15) used by Silver and Chan yielded (ϕ, δt) for Red Lake, Ontario and Yellowknife, NWT of (75^0, 1.75 s) and (48^0, 1.10 s). That is, the calculated direction is significantly different and the degree of apparent anisotropy is much less.
(ii) High quality recordings are required at several stations before reliable inferences can be made.
(iii) Since the SKS phase is only useful in the range 84^0 - 110^0, a distance range where the P phase is of low amplitude, operating in a triggered mode is not an effective procedure, particularly with the EDA instruments which have a maximum of 6 Mb of memory. Recorders are now available which have a storage capacity of 100 Mb (Geotech and RefTek). These allow continuous recording of one months data at the sample rates required for this long period (~5 s) phase.
(iv) P.G. Silver (personal communication) indicates that during an experiment in Wisconsin he recorded 6 usable events in 4 months. This number is required to provide confidence in the observations. In the noisy prairie environment, larger magnitude events are required. Further, recording outside the seismically quiet summer months will raise the usable threshold. For the SKS phase a recording period of at least 8 months is therefore desirable.

Summary and Recommendations

The overall objectives of this initial experiment were as follows:
(i) to allow definition of technical problems;
(ii) to provide sufficient data to test each of the techniques and to evaluate whether anomalies exist;
(iii) to provide an improved estimate of the time period and number of stations required to provide an adequate data set for a full-scale analysis program.

The technical problems to be investigated were to determine the suitability of the PRS-4 recorders to attain the scientific objectives of the program and where necessary to make the appropriate modifications:

(i) To record the broadband output of the Guralp seismometers for the teleseismic deconvolution study, modifications as detailed in Appendix A were made to extend the lower corner of the system response from 0.5 to 0.05 Hz.
(ii) To provide adequate timing for the P wave travel time residual investigation, we have found that recording of the WWVB time signal and appropriate processing of time signal waveform is an excellent solution to the problem. The required modifications to the PRS-4 recorder and the processing technique is detailed in Appendices A and B, respectively.
(iii) To record the P waveforms on the sediments of Saskatchewan, both for the traveltime residual investigation and teleseismic deconvolution study, the LithoSEIS parameters as provided in Table A1 are fully satisfactory. Although the average false alarm rate is ~40%, this allows 2 months recording without uploading.
(iv) Due to the limited memory, the PRS-4 recorders are unsuitable for the SKS experiment. Recording with the RefTek or Geotech SDAS-100 systems, both of which allow 100 Mb storage on hard disk is the appropriate approach. This will allow approximately one month of continuous and unattended recording. (Note: NSERC has granted funds to R.M. Ellis to purchase 5 new digital recorders. The application was for the EDA PRS-4 units to provide compatibility with the GSC instruments. In view of the results of this

experiment, his intent is to purchase either the RefTek or Geotech systems by supplementing the NSERC equipment grant.) In a future program in which the 3 types of analyses of this experiment are envisaged, the Guralp seismometers should be linked to both PRS-4 and RefTek or Geotech recorders.

The preliminary results from the traveltime experiment are as follows:
(i) Large traveltime residuals (several 100 ms) have been observed between stations implying large crustal and upper lithosphere velocity structure anomalies.
(ii) Based on the spatial variations observed, station spacing of ~100 km is desirable; a 300 - 400 km array with ~16 stations would provide good areal coverage and is technically manageable.
(iii) To acquire an adequate data set, at least 8 months of full operation should be planned.

Analysis of data from the teleseismic deconvolution perspective, indicates:
(i) The shear wave velocity structure will be interpretable into the upper mantle.
(ii) Development (or acquisition) of a ray tracing algorithm which accounts for finite Q is necessary.
(iii) The field program should be planned for one year's duration.

The SKS experiment is feasible in this environment but requires:
(i) Recorders with large data capacity (~ 100 Mb), e.g. RefTek 72 or Geotech SDAS-100.
(ii) A recording period of ~8 months is recommended. For this period, the sensible procedure is to record the output of the Guralp seismometers on both PRS-4 (for traveltime and receiver function studies) and on the second recorder at a lower sampling rate (for SKS analysis).

The results of this feasibility study show that no technical barriers exist with respect to a combined traveltime, teleseismic deconvolution and anisotropy experiment. The length of the experiment should be one year to acquire a suitable data set; a timely sequence of earthquakes may allow the SKS/anisotropy experiment to be of shorter duration. A combined interpretation of these techniques should allow a significantly improved velocity characterization of the crust and upper mantle in the target region. To maximize the effectiveness of the experiment, input from the various stakeholders with a geological perspective is required.

REFERENCES

Ammon, C. J., G. E. Randall, and G. Zandt (1990). On the non-uniqueness of receiver function inversions, J. Geophys. Res., **95,** 15,303-15,318.

Ammon, C. J. (1991). The isolation of receiver effects from teleseismic P waveforms, Bull. Seism. Soc. Am., **81**, 2504-2510.

Babuska, V., J. Plomerova, and J. Sileny (1984a). Spatial variations of P residuals and deep structure of the European lithosphere, Geophys. J. R. Astr. Soc., **79**, 363-383.

Babuska, V., J. Plomerova, and J. Sileny (1984b). Large-scale oriented structures in the subcrustal lithosphere of Central Europe, Ann. Geophysicae, **B2**, 649-662.

Babuska, V., J. Plomerova, and J. Sileny (1987a). Structural model of the subcrustal lithosphere in Central Europe, *In* Composition, Structure and Dynamics of the Lithosphere-Asthenosphere System Geodyn. Ser., **16**, edited by K. Fuchs and C. Froidevaux, American Geophysical Union, Washington, D.C., 239-251.

Babuska, V., J. Plomerova, and E. Spassov (1987b). Deep structure of the lithosphere beneath the territory of Bulgaria, Studia Geophy. et Geod., **31**, 266-283.

Bowman, J. R. and M. Ando (1987). Shear-wave splitting in the upper-mantle wedge above the Tonga subduction zone, Geophys. J. R. Astr. Soc., **88**, 25-41.

Buchbinder, G. and G. Poupinet (1977). P-wave residuals in Canada, Can. J. Earth Sci., **14**, 1292-1304.

Cassidy, J. F. (1991). Teleseismic receiver function analysis of the crust and upper mantle of southwestern British Columbia, Ph.D. thesis, Univ. of British Columbia, 174p.

Collerson, K.D., J.F. Lewry, M.E. Bickford, and W.R. Van Schmus, 1990. Crustal evolution of the buried Precambrian of southern Saskatchewan: implications for diamond exploration, *In* Modern Exploration Techniques, L.S. Beck, ed., Saskatchewan Geological Society, Special Publication 10, pp. 150-165.

Davies, D., rapporteur (1968). Seismic methods for monitoring underground explosions, International Institute for Peace and Conflict Research (SIPRI), Stockholm, 130p.

Dawson, J.B. (1989). Geographic and time distribution of kimberlites and lamproite: relationships to tectonic processes. *In* Kimberlites and related rocks, **1**, J. Ross, ed., 323-342, Proceedings of the Fourth International Kimberlite Conference, Perth, 1986, Geol. Soc. Australia Special Publication 14, Blackwell, Oxford.

Eggler, D.H. (1989). Kimberlites: how do they form? *In* Kimberlites and related rocks, **1**, J. Ross, ed., 489-504, Proceedings of the Fourth International Kimberlite Conference, Perth, 1986, Geol. Soc. Australia Special Publication 14, Blackwell, Oxford.

Ellis R. M., Z. Hajnal, J. Amor, T. Mulder, N. Dotzev, and R. D. Meldrum (1992). Investigation of the Properties of the Lithosphere Using Teleseismic Waves, A Preliminary Report for Energy Mines and Resources Canada and Cameco Corporation, 12p.

Helmberger, D., and R.A. Wiggins (1971). Upper mantle structure of mid-western United States, J. Geophys. Res. **76**, 3229-3245.

Jeffreys, H. and K. E. Bullen (1940). Seismological tables, British Association for the Advancement of Science, London, 50 pp.

Haggerty, S.E. (1986). Diamond genesis in a multiple-constrained model, Nature, **320**, 34-38.

Kennett, B. L. N. (1991). IASPEI 1991 Seismological Tables. Research School of Earth Sciences Australian National University, Canberra, Australia, 167 pp.

Kirkley, M.B., J.J. Gurney and A.A. Levinson (1992). Age, origin and emplacement of diamonds: a review of scientific advances in the last decade, *CIM Bull.*, **84**, 48-57.

Langston, C. A. (1977). The effect of planar dipping structure on source and receiver responses for constant ray parameter, Bull. Seism. Soc. Am., **67**, 1029-1050.

Langston, C. A. (1979). Structure under Mount Rainier, Washington, inferred from teleseismic body waves, J. Geophys. Res., **84**, 4749-4762.

Meyer, H.O.A. (1985). Genesis of diamond: a mantle saga, Am. Mineralogist, **70**, 344-345.

Moore, R.O. and J.J. Gurney (1985). Pyroxene solid solution in garnets included in diamond, Nature, **318**, 553-555.

Morel-à-l'Hussier, P., A.G. Green, A.G. Jones, T. Latham, J.A. Majorowicz, M.J. Drury, and M.D. Thomas, 1990. The crust beneath the intracratonic Williston Basin from geophysical data, *In* The Potential of Deep Seismic Profiling for Hydrocarbon Exploration, B. Pinet and C. Bois, ed., Editions Technip, Paris, pp. 141-160.

Owens, T. J., G. Zandt, and S. R. Taylor (1984). Seismic evidence for an ancient rift beneath the Cumberland Plateau, Tennessee: a detailed analysis of broadband teleseismic P waveforms, J. Geophys. Res., **89**, 7783-7795.

Owens, T.J., S.R. Taylor, and G. Zandt (1987). Crustal structure at regional seismic test network stations determined from inversion of broadband teleseismic P waveforms, Bull. Seism. Soc. Am., **77**, 631-662.

Owens, T. J., and R. S. Crosson (1988). Shallow structure effects on broadband teleseismic P waveforms, Bull. Seism. Soc. Am., **78**, 96-108.

Owens, T.J., R.S. Crosson and M.A. Hendrickson (1988). Constraints on the subduction geometry beneath western Washington from broadband teleseismic waveform modelling, Bull. Seism. Soc. Am., **78**, 1319-1334.

Paulssen, H.(1988). Evidence for a sharp 670-km discontinuity as inferred from P-to-S converted waves, J. Geophys. Res., **93**, 10,489-10,500.

Richardson, S.H. (1986). Latter-day origin of diamonds of eclogitic paragenesis, Nature, **322**, 623-626.

Richardson, S.H., J.J. Gurney, A.J. Erlank and J.W. Harris (1984). Origin of diamonds in old enriched mantle, Nature, **310**, 198-202.

Richardson, A.J. Erlank, J.W. Harris and S.R. Hart (1990). Eclogitic diamonds of Proterozoic age from Cretaceous kimberlites, Nature, **346**, 54-56.

Silver, P. G. and W. W. Chan (1988). Implications for continental structure and evolution from seismic anisotropy, Nature, **335**, 34-39.

Silver, P. G. and W. W. Chan (1991). Shear Wave Splitting and Subcontinental Mantle Deformation, J. Geophys. Res., **96**, 16,429-16,454.

Wickens, A. J. and G. G. R. Buchbinder (1980). S-wave residuals in Canada, Bull. Seism. Soc. Am., **70**, 809-822.

APPENDIX A

FIELD OPERATION NOTES

PRS-4 Triggering

In LithoSEIS, the PRS-4 trigger parameters are set on page 2 of the deployment definition screens (PREPARE:PLAN:DEPLOYMENTS, Pg. 2 of 5). The preferred values of these parameters are shown in Table A1 for broadband, short period, and SKS deployments. Triggering is on the vertical seismometer in all cases. The second set of SKS parameters (TF13) is currently active and was instigated by the failure of the initial settings (TF08) to trigger on a M = 6.5 event from India.

The sample rate of 50 Hz was selected to provide adequate resolution for P residual studies. While a sample rate lower than 30 Hz would have been preferred for SKS recording, LithoSEIS 4.0 will not generate the decimated lowpass filter required for an adequate trigger. The trigger filter designs all reflect the presence of a strong 3 s microseismic background at all sites. TF07 was used on several broadband deployments to reduce the possibility of triggering on high frequency noise due to agricultural activity, but in general, it appears less reliable than TF02. In particular, it reduces false triggers due to agricultural noise and is suitable for higher frequency events, but it does not appear to be as effective a trigger for lower frequency onsets. For short period recording, TF07 is adequate although an enhanced low frequency response would be preferable. As yet a replacement filter has not been adequately tested to determine its overall effect on the triggering.

The STA and LTA are approximations to those used by Cassidy (1991). No trials were made with alternatives, although it may be that noise triggers due to agricultural activity could be reduced with a shorter LTA.

The trigger ratios indicated were found to be adequate. It is noted that if one wishes to reduce the number of lower signal-to-noise ratio events by increasing the ratios to greater than 10, LithoSEIS 4.0 will 'crash' if the ratio is entered directly on the Pg. 2 deployment screen and downloaded; however, double digit ratios can be set after downloading using the LithoSEIS Monitor function EXECUTE: MONITOR: MONITOR: F4 [MODIFY PARAMS].

Note that as shown, the high band and low band filters entries do not follow the usual LithoSEIS convention.

Trigger Performance: False trigger rates vary from station to station depending on local noise but are typically of the order of 40%. (This figure neglects false triggers due to mass recentres on the Guralp seismometers induced by ambient temperature changes and also those due to the loss and recovery of AC power).

Seismograph Siting

With the exception of USK and DLK which are located in the University of Saskatchewan seismic vault and in a storage building at Deschambault Lake respectively, the seismographs are installed in unused or abandoned farm buildings with AC power available. As the farms are operational and grain storage sheds are often present (e.g. at FLX, TSD, RAY), the level of noise due to agricultural activity increases during certain periods but generally only for a few days.

At RAY and TSD, it was found that 4 inches of R10 placed over the seismometers and feedback electronics minimized temperature induced mass recentres and thus false triggers. At DLK and FLX, burial of the systems in portable vaults virtually eliminated the problem. A summary of the siting details is provided in Table A2.

PRS-4 Hardware Modifications

Channel 4: PRS-4's are manufactured with an input filter on channel 4 intended to rectify and integrate radio time ticks such as CHU and WWV. These filter components (two diodes CR7 and CR12, resistor R76, and capacitor C63 on the CPU card), were removed and replaced by a single

TABLE A1

LithoSEIS Trigger Parameters

	Broadband	Short Period	SKS	SKS (trial)
Sample Rate (Hz)	50	50	30	30
STA constant (s)	2.54	2.54	2.10	2.10
LTA constant (s)	102.2	102.2	85.0	85.0
STA/LTA ratio	6.0	9.5	15.0	9.5
IIR CODE	**TF02**	**TF07**	**TF08**	**TF13**
Lo Pass (Hz)	1.10	1.10	0.80	0.60
Q	14.0	50.0	20.0	18.0
Hi Band (Hz)	0.50	0.70	0.50	0.50
Q	24.0	50.0	20.0	18.0
Lo Band (Hz)	1.80	1.90	1.70	1.00
Q	8.0	20.0	20.0	12.0
Decimation				
Lo -> IIR1	2	2	2	2
IIR2	1	1	1	1
Sta	1	1	1	1

TABLE A2

Details of Station Sites

Station	Type	Seismometer Location	Equipment Site
DLK	broad band	buried vault on bedrock	school building
FLX	broad band	buried vault in yard	abandoned grainery
GRY	short period	buried in cellar	abandoned farm house
HLB	short period	basement floor	vacant house
RAY	broad band	cement floor	unused farm building
SND	short period	buried in cellar	abandoned farm house
TSD	broad band	cement floor	abandoned vehicle garage
USK	broad band	concrete pier	underground vault

calibration reference waveforms, as well as an undistorted WWVB time code waveform used to periodically rate the PRS internal clock.

Channels 1, 2, 3: As received from the GSC, the PRS-4 seismic channels had a high pass corner at 0.5 Hz, inappropriate to our application. Accordingly, the filter corner was moved to 0.05 Hz by replacing two resistors and one capacitor on each channel. In particular, C25 on the CPU card and C7 and C107 on the Dual 100 Hz card were changed from 0.56 mF to 4.7 mF. R51 and R52 on the CPU card and R20, R21, R120, and R121 on the Dual 100 Hz card were changed from 499 kΩ to 681 kΩ. These changes introduced large offsets on the associated operational amplifiers in some of the PRS's, namely U31 on the CPU card and U5 and U105 on the Dual 100 Hz card. Scrupulous cleansing of the boards reduced the offsets to reasonable levels although not all could be trimmed to zero. Channel 1 was consistently the worst offender and leakage currents through R51 are the suspected cause. A leakage current of 3 nanoamps through R51 exceeds the offset null capability of the circuit. A +12 volts trace on the circuit board within 1 mm of R51.

Calibrations

With the PRS-4 channel 4 modified to permit direct recording of the input waveform, calibration of both the PRS-4 alone and the PRS-Guralp broadband system is facilitated.

Discrete frequency amplitude and phase calibrations of PRS-4's were obtained by feeding the output of a wave generator simultaneously into the 4 inputs of an active PRS and inducing calibration recording cycles. Spectral analysis of the resulting waveforms yields the calibration data as plotted in Fig. A1.

Similarly, when the calibration current for Guralp seismometers is passed through the 10kΩ shunt resistor on the PRS channel 4 input, the amplitude and phase calibrations of the entire systems can be obtained. Typical response curves for one channel of a seismograph are shown in Fig. A2. Differences in response between channels are minimal.

The increasing phase lag at higher frequencies in both PRS-4 and system calibrations is a consequence of the the electronic anti-alias filters through which the channels 1,2, and 3 data is passed.

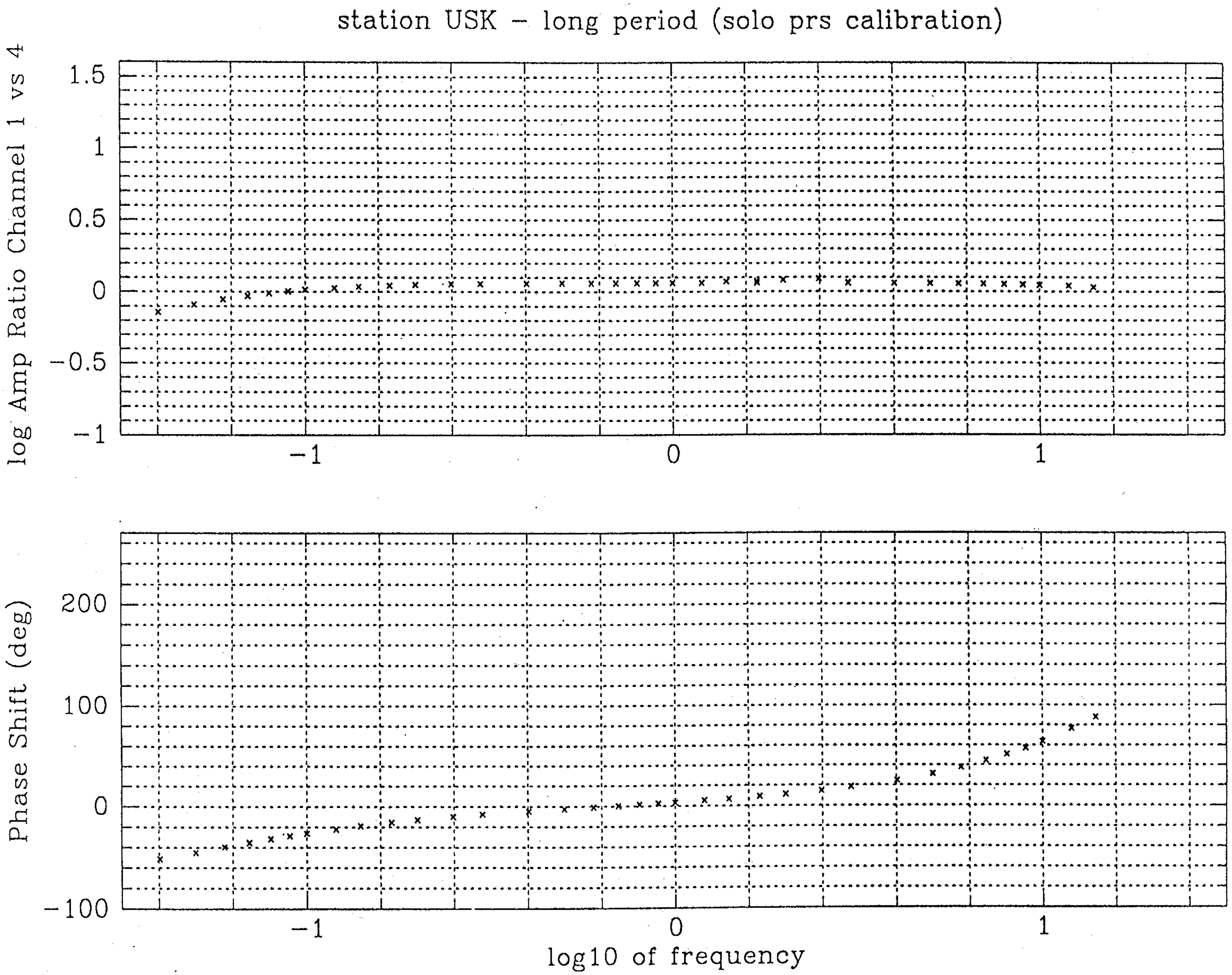

Fig. A1. Amplitude and phase calibration of PRS-4 serial #0075, channel 1.

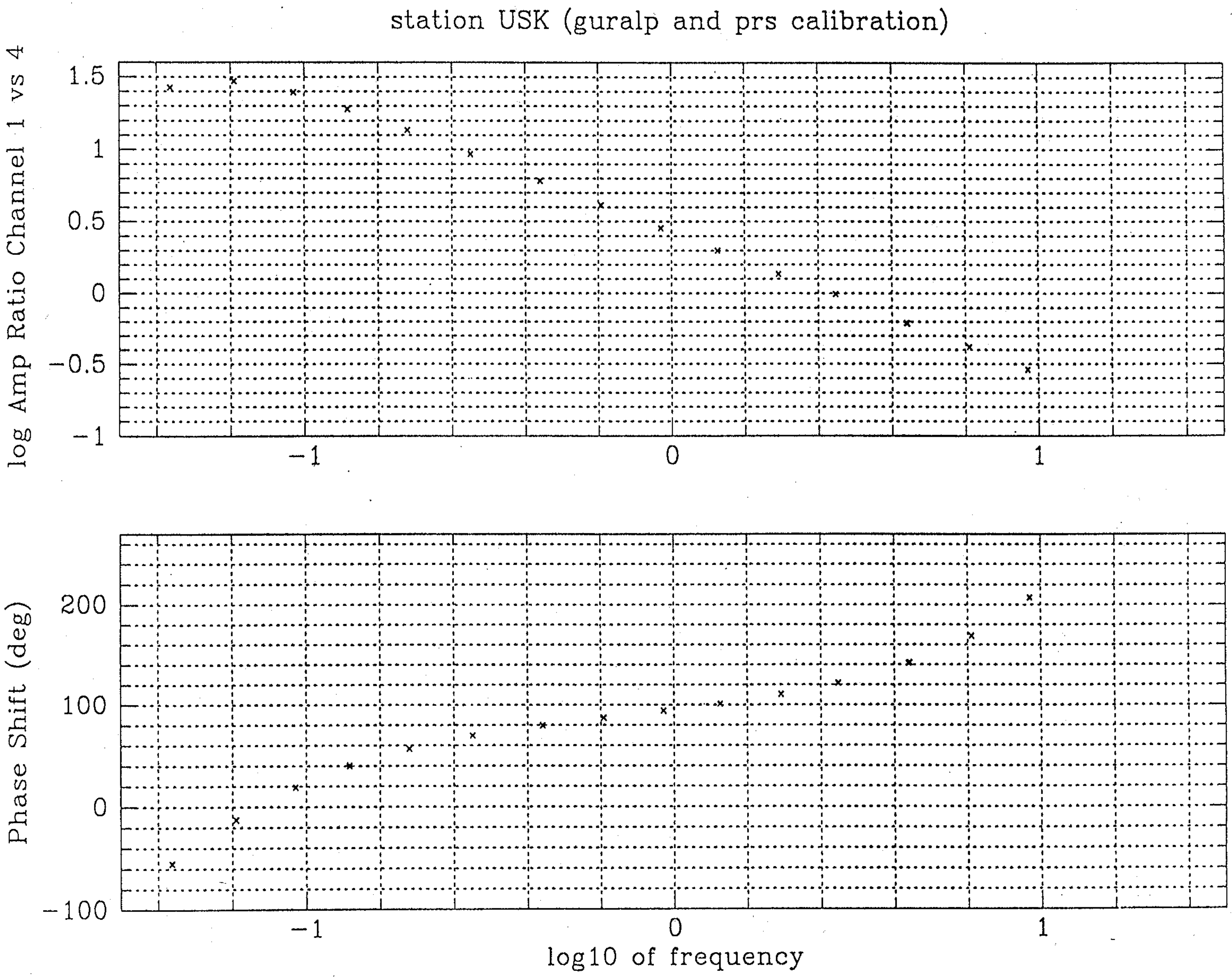

Fig. A2. Amplitude and phase calibrations of complete USK broadband seismograph, channel 1.

APPENDIX B

TIMING CORRECTIONS

Introduction

To obtain traveltime residuals for each station with respect to standard tables or for interstation traveltime comparisons accurate timing is required. The internal clock of the PRS-4 system is based on a crystal oscillator with a rated stability of 2 x 10^{-7} over the operational range and an aging rate of 10^{-8} per day. This clock is rated during both the download and upload procedures which allows a linear correction to be applied. However in a typical deployment of one to two months, deviations from this linear interpolation of 10's to 100's of ms occur. In order to minimize the interpolation interval and thus the errors due to the linear drift assumption, each station was programmed to record WWVB for 20 s on the hour at 7 hour intervals (later extended to 13 hours). These intervals were chosen to avoid recording at the same time each day and possibly encountering consistently weak signals. Fig. B1 is an example of the time variation following removal of the linear drift over the deployment interval. It is noted that the deviations from linearity are small over intervals of several days.

Fig. B2 is an example of a moderately noisy WWVB time signal which is composed of a series of pulses of varying duration spaced at 1 s intervals. To obtain an accurate time correction requires the accurate determination of the leading edge, a problem complicated by both noisy signals and the finite rise time of the pulse. Once this is accomplished, linear interpolation is used between the 7 (or 13) hour calibration times.

Timing Calibration Procedure

Since the leading edge of the WWVB signal is periodic, the signal-to-noise can be improved by a simple stacking procedure. The result of applying this procedure to the signal of Fig. B2 is shown in Fig. B3. The ragged trailing edge results from the varying pulse widths.

Since the onset of the edge is difficult to determine directly, it was decided to use the mid-point in amplitude of the edge as the onset time. Two sample points adequately define the leading edge and its slope since the WWVB rise time is ~30 ms. A 9-point averaging filter was applied to obtain a smoothed signal from which the maximum and minimum was extracted and hence the amplitude of the midpoint and its time. (We note that the 9-point filter is the maximum length which fits within the minimum pulse width). The time correction is then the difference from the start of the recorded window to the mid-point time plus whole second corrections, if applicable, which are obtained by relating the measured time correction to the standard linear value.

Errors

An estimate of the error in the time correction was made by calculating the standard deviation of each point of the stacked data. The standard deviations of the points used to estimate the time correction were then used to estimate the uncertainties in these corrections by adding the standard deviations to each point. The WWVB time correction was considered unusable if the uncertainty in the correction exceeded 5 ms. This criterion results in rejection of 1.5% of the WWVB time corrections.

This method of edge detection assumes that the width of the WWVB edge is greater than the sampling interval. While the rise times of the output pulses of the receivers are significantly shorter than the sample interval (see WWVB Receiver Corrections), the FIR decimation filter in the PRS-4 ensures that the recorded rise time meets this requirement. This can be demonstrated by taking the two stacked points from either side of all the interpolated time corrections from an entire deployment and plotting them, with the non-linear correction applied, to obtain an image of the recorded WWVB edge. Fig. B4 shows such an image and is the response of the decimation filter to the sharp WWVB edge. The slight 's' shape of the edge results from the fact that the two sample points used to determine the mid-point amplitude are not always both on the edge. However, the estimated error due to this effect is ~1-2 ms and has therefore been neglected.

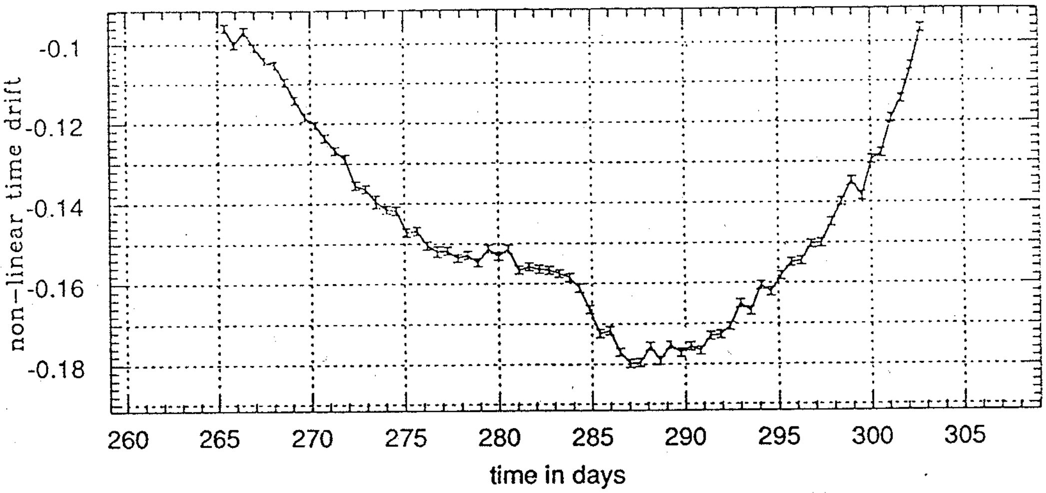

Fig. B1. PRS-4 clock drift at RAY following removal of a linear component over the deployment interval.

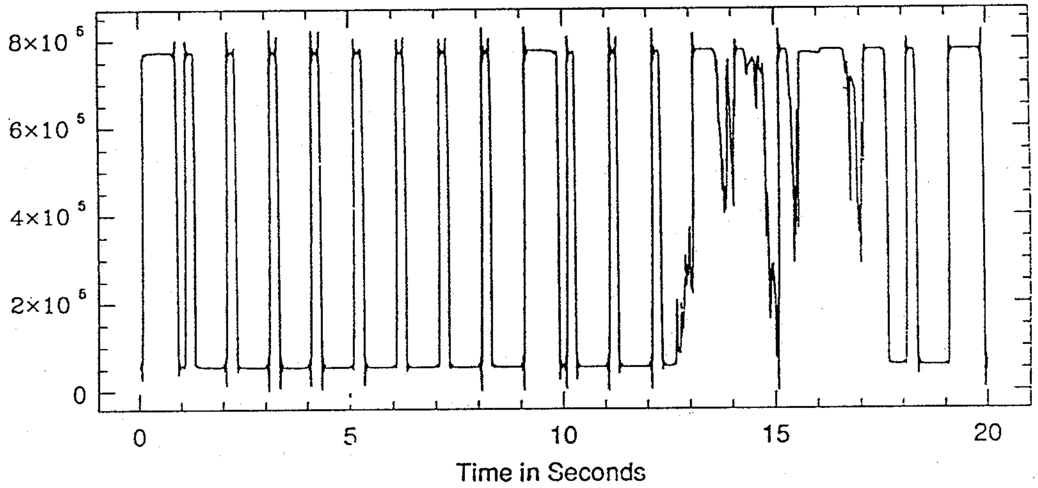

Fig. B2. Example of 20 s recording of WWVB time signal.

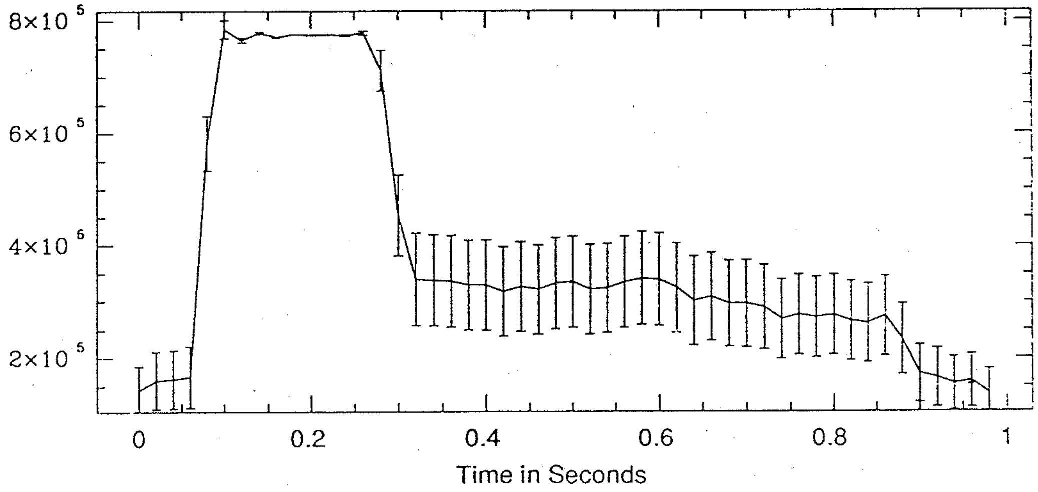

Fig. B3. Waveform resulting from stacking of the WWVB signal of Fig. B2. This waveform is yields a correction of -0.074 +/- 0.003 ms.

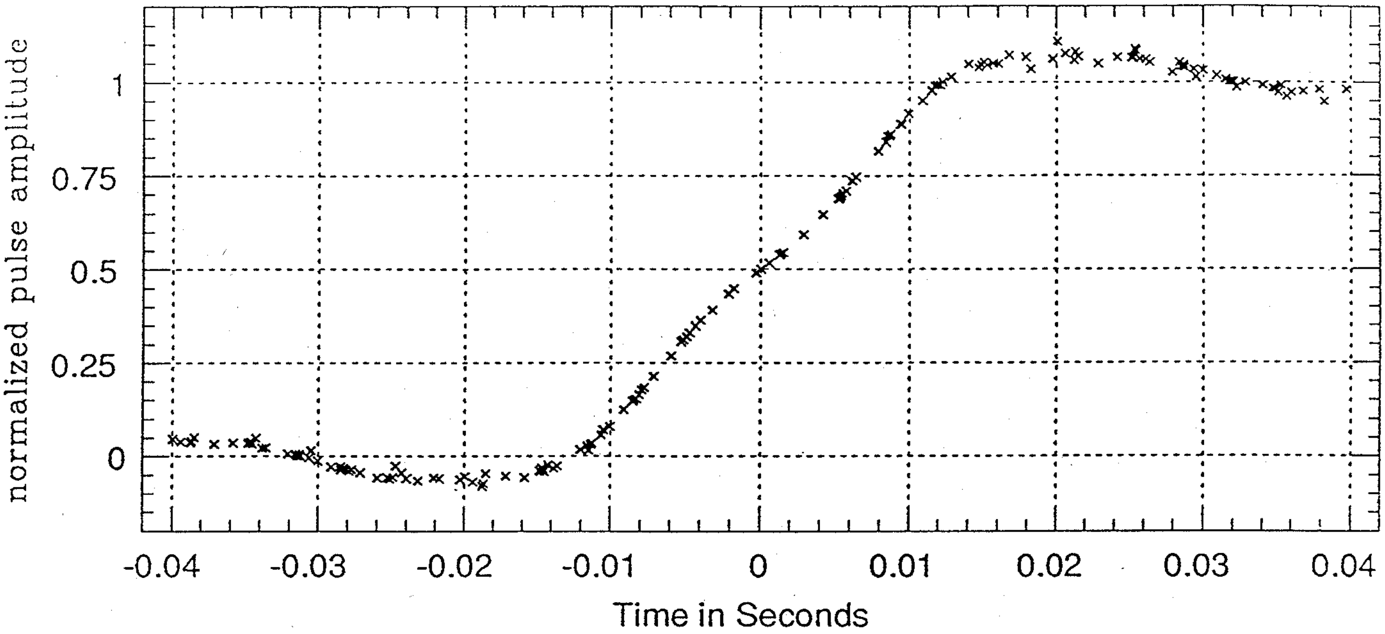

Fig. B4. Image of the recorded WWVB edge obtained by stacking two points on either side of the interpolated time correction at SND.

Absolute time corrections

Absolute timing requires that receiver delays and time from the onset of the WWVB edge to the mid-point be known. Receiver rise times and delays relative to short wave WWV receiver output ticks (which were the reference for PRS download and upload) were measured in the field for each station and are tabulated in Table B1. As the rise times indicated in Table B1 are short compared to the sample interval of 20 ms, it is seen that the time from WWVB onset to mid-point of the edge (Figure B4) is determined by the FIR decimation filter in the PRS-4 software. The characteristics of this filter are described in the PRS-4 technical notes (SCINTREX, 1990) That material provides the basis for determining the onset to mid-point delay should absolute time be required.

PRS-4 Clock Start Error

The drift curve of Fig. B1 shows non-linear PRS-4 clock corrections of the order of -95ms at download and upload time, implying a timing error associated with the PRS-4 clock rating procedure under LithoSEIS. The source of this offset is presumed to be the computation time of the decimation filter which delays all channels with respect to the PRS-4 clock. This is easily demonstrated by recording, with a PRS-4, the edge from a clock initially used to start the recorder.

SCINTREX (1990). PRS-4: Portable Recording Seismograph/Accelerograph, Notes presented by B. Markle at LithoSEIS Workshop, Ottawa, January 1992.

Table B1

WWVB Receiver Time Corrections

Station	Receiver type	Rise time (ms)	Delay re WWV (ms)
DLK	True Time	0.75	14
FLX	True Time	*	12
GRY	Develco (detected)	7	5
HLB	Develco (detected)	6	4
RAY	True Time	0.018 (?)	13
SND	Develco (detected)	7	4
USK	True Time	0.75	14
TSD	Develco (sliced)	<1	4

* - Rise time should be assumed to be 0.75 ms as for DLK and USK

APPENDIX C

TABLE C1

List of earthquakes that could be used for $P-$wave travel time analysis.

No.	Origin time Y.D.h.m.	Depth (km)	M	BAZ°	Δ°	Station names
1	91 184 06 08	57	4.7	154.1	44.2	TSD
				150.4	44.2	USK
3	91 185 10 32	33	5.0	301.2	78.3	FLX
				303.4	79.6	USK
				305.1	80.4	TSD
5	91 186 10 58	456	5.6	312.4	61.9	FLX
				315.0	63.4	TSD
				313.9	62.8	USK
7	91 187 12 19	85	6.3	147.5	71.3	TSD
				145.0	71.5	USK
				141.7	72.1	FLX
10	91 190 05 54	101	5.3	146.9	79.4	TSD
				144.7	79.7	USK
				141.7	80.2	FLX
11	91 190 06 53	33	5.5	120.5	41.5	TSD
				117.0	42.5	USK
				112.8	44.0	FLX
12	91 191 05 52	97	5.5	308.9	65.4	FLX
				311.9	67.1	TSD
				310.6	66.4	USK
18	91 193 00 40	10	4.7	151.6	50.4	TSD
				148.3	50.6	USK
				144.0	51.0	FLX
25	91 194 12 15	40	5.7	308.2	57.0	FLX
				309.5	58.0	USK
26	91 195 09 09	223	6.4	4.0	91.0	TSD
				2.0	91.8	USK
				359.3	92.6	FLX

No.	Origin time Y.D.h.m.	Depth (km)	M	BAZ°	Δ°	Station names
27	91 195 10 03	10	5.0	179.4	83.5	FLX
				182.2	84.4	USK
31	91 196 12 22	33	5.5	307.3	61.5	FLX
				308.9	62.6	USK
32	91 196 18 09	0.0	5.3	212.8	80.4	TSD
				210.7	79.0	USK
36	91 199 11 56	13	5.8	37.0	72.3	TSD
				35.3	73.7	USK
				33.0	75.5	FLX
49	91 215 08 33	16	5.4	315.6	86.0	TSD
				313.8	85.4	USK
50	91 216 07 45	33	5.2	152.2	56.9	TSD
				149.2	57.0	USK
51	91 217 06 05	31	5.4	237.6	91.9	FLX
				240.1	94.1	USK
52	91 217 11 08	33	5.1	300.8	44.1	FLX
				301.6	45.5	TSD
				301.6	45.5	USK
53	91 218 14 49	34	5.8	306.7	73.4	FLX
				308.8	74.6	USK
				310.3	75.2	TSD
				310.3	74.2	DLK
54	91 221 01 13	254	4.7	311.9	65.9	FLX
				313.6	66.8	USK
59	91 225 02 11	10	5.3	63.9	38.9	DLK
				61.5	40.2	TSD
				57.5	44.0	FLX
				59.7	41.8	USK
60	91 226 12 53	229	5.7	289.8	35.2	FLX
				299.0	36.6	USK
				297.0	36.9	DLK
				299.1	37.6	TSD

No.	Origin time Y.D.h.m.	Depth (km)	M	BAZ°	Δ°	Station names
62	91 227 23 27	105	5.4	296.7	36.6	FLX
				297.1	38.0	USK
				295.4	38.4	DLK
				297.4	39.0	TSD
64	91 229 06 18	10	5.1	134.6	50.8	TSD
				131.4	51.4	USK
				136.4	52.0	DLK
				127.3	52.5	FLX
66	91 229 12 39	64	5.3	125.8	53.8	TSD
				119.1	56.0	FLX
				122.9	54.7	USK
71	91 230 10 52	579	5.4	242.7	91.3	FLX
				245.3	93.5	USK
73	91 230 21 52	46	5.4	152.8	89.1	TSD
				150.8	89.2	USK
75	91 231 06 05	44	5.7	353.9	78.2	DLK
				351.9	80.7	USK
				349.6	81.2	FLX
79	91 238 10 01	10	5.3	143.4	38.4	TSD
				139.5	38.7	USK
80	91 238 14 59	45	5.8	308.7	66.8	FLX
				311.5	67.4	DLK
				311.8	68.5	TSD
				310.4	67.8	USK
84	91 244 06 51	10	5.2	16.8	39.8	DLK
				15.5	42.9	USK
86	91 246 08 44	23	5.9	309.1	77.4	USK
				310.8	77.0	DLK
87	91 246 09 05	10	6.2	189.7	70.2	USK
				192.5	73.2	DLK

No.	Origin time Y.D.h.m.	Depth (km)	M	BAZ°	Δ°	Station names
88	91 246 11 56	10	5.8	189.7	70.2	USK
				192.5	73.3	DLK
96	91 258 06 39	10	5.6	186.4	69.1	FLX
				189.7	70.2	USK
				192.1	71.2	TSD
				192.5	73.2	DLK
				193.6	69.2	GRY
98	91 261 09 48	5	5.7	158.7	38.2	RAY
				156.2	39.5	USK
				161.8	41.4	DLK
				161.3	37.2	GRY
99	91 262 01 41	37	5.5	309.6	58.0	USK
				311.1	59.5	RAY
				312.3	60.8	GRY
101	91 264 15 19	33	5.9	239.4	86.9	FLX
				242.0	89.1	USK
				243.5	89.8	RAY
				243.9	90.1	TSD
				244.4	91.9	DLK
				245.0	90.6	GRY
				242.2	89.8	HLB
				243.5	89.8	SND
102	91 265 06 32	33	5.5	309.4	56.6	USK
				309.0	56.1	HLB
				312.1	59.4	GRY
109	91 273 00 21	580	6.0	240.9	93.8	FLX
				243.5	96.0	USK
				245.4	97.7	TSD
				243.8	96.6	HLB
				246.2	97.5	GRY
115	91 279 10 12	33	4.9	296.7	41.5	HLB
				297.7	41.9	USK
				300.8	44.7	GRY

No.	Origin time Y.D.h.m.	Depth (km)	M	BAZ°	Δ°	Station names
117	91 279 16 48	144	5.4	145.1	65.2	USK
				148.9	66.5	DLK
				148.7	62.6	GRY
				147.2	65.7	SND
119	91 281 03 31	147	6.0	311.1	62.7	DLK
				310.3	63.1	USK
				310.0	62.5	HLB
				313.1	65.9	GRY
				311.8	64.6	RAY
136	91 292 21 23	19	6.5	358.1	94.7	DLK
				357.6	96.7	TSD
				355.5	97.3	USK
				352.6	97.9	FLX
				357.0	96.0	SND
153	91 298 10 39	111	5.7	309.7	66.1	FLX
				312.5	66.5	DLK
				311.4	67.1	USK
				312.8	67.7	TSD
				312.9	68.6	RAY
				314.2	69.8	GRY
				312.1	66.9	SND
156	91 299 02 27	193	5.8	295.3	86.1	USK
				297.5	86.5	DLK
				296.9	87.6	RAY
				297.2	87.1	TSD
				292.9	84.5	FLX
				296.6	86.4	SND
				298.3	88.9	GRY
163	91 300 16 17	178	5.6	145.7	80.2	RAY
				144.1	81.6	USK
				146.3	81.3	TSD
				141.2	82.2	FLX
				146.9	82.8	DLK
				147.3	79.0	GRY
				145.7	82.1	SND

No.	Origin time Y.D.h.m.	Depth (km)	M	BAZ°	Δ°	Station names
166	91 303 10 35	58	5.7	240.1	86.2	FLX
				242.6	88.4	USK
				244.2	89.0	RAY
				244.6	90.0	TSD
				245.1	91.2	DLK
				245.7	89.9	GRY
173	91 314 08 20	33	5.1	147.7	46.1	USK
				149.8	44.7	RAY
				151.3	45.9	TSD
				153.9	47.5	DLK
176	91 315 17 46	33	5.5	173.0	33.5	FLX
				182.0	33.3	RAY
				178.7	34.2	USK
				182.8	34.9	TSD
				183.5	37.0	DLK
				185.3	32.8	GRY
177	91 315 22 34	23	5.9	298.8	81.4	FLX
				303.2	82.9	DLK
				301.2	82.7	USK
				302.9	83.6	TSD
				302.7	84.2	RAY
				301.2	82.3	HLB
				302.3	82.9	SND
				304.2	85.6	GRY
179	91 317 13 21	148	5.0	144.5	53.6	RAY
				145.8	54.8	TSD
				142.7	55.0	USK
				146.4	52.4	GRY
				145.2	55.6	SND

No.	Origin time Y.D.h.m.	Depth (km)	M	BAZ°	Δ°	Station names
180	91 317 19 20	308	5.4	307.5	76.8	FLX
				311.4	77.5	DLK
				309.6	77.9	USK
				311.3	78.6	TSD
				311.1	79.4	RAY
				309.6	77.4	HLB
				310.6	77.8	SND
				312.5	80.7	GRY
181	91 317 20 27	29	5.3	148.0	53.8	TSD
				144.8	54.1	USK
				148.7	51.5	GRY
184	91 320 11 12	10	5.3	169.4	57.0	FLX
				173.3	57.5	USK
				177.8	55.8	GRY
				175.4	58.8	SND
187	91 323 22 28	21	6.5	144.8	51.7	RAY
				146.1	52.9	TSD
				143.0	53.2	USK
				147.6	54.4	DLK
				138.8	53.8	FLX
				146.8	50.6	GRY
				145.6	53.7	SND
				143.8	54.0	HLB
195	91 330 10 41	69	5.8	297.6	40.0	FLX
				298.3	41.4	USK
				298.7	42.4	TSD
				300.0	42.9	RAY
				297.3	41.0	HLB
				297.7	41.6	SND
				301.4	44.2	GRY

No.	Origin time Y.D.h.m.	Depth (km)	M	BAZ°	Δ°	Station names
198	91 330 19 40	55	6.2	310.0	67.8	FLX
				312.9	68.3	DLK
				311.8	68.8	USK
				313.1	69.5	TSD
				313.2	70.3	RAY
				311.6	68.2	HLB
				312.5	68.7	SND
				314.6	71.6	GRY
199	91 331 05 03	35	5.9	307.8	57.3	FLX
				309.6	58.1	DLK
				309.1	58.4	USK
				310.1	59.1	TSD
				310.6	59.9	RAY
				308.8	57.9	HLB
				309.4	58.4	SND
				311.9	61.2	GRY
201	91 332 17 19	14	5.7	21.5	85.8	DLK
				19 1	89.0	USK
				20.4	87.0	SND
210	91 341 11 59	52	5.5	308.8	62.0	USK
				310.3	63.5	RAY
				308.5	61.4	HLB
211	91 341 16 34	45	5.4	308.8	61.9	USK
				310.3	63.4	RAY
				308.5	61.4	HLB
				309.2	61.9	SND
215	91 342 14 09	33	5.3	307.2	60.9	FLX
				308.8	62.0	USK
				308.5	61.4	HLB
				309.2	61.9	SND
				311.6	64.8	GRY

No.	Origin time Y.D.h.m.	Depth (km)	M	BAZ°	Δ°	Station names
221	91 345 17 03	10	5.9	186.5	69.1	FLX
				191.8	70.0	RAY
				189.8	70.2	USK
				192.1	71.2	TSD
				192.6	73.2	DLK
				193.7	69.2	GRY
				190.0	71.4	HLB
				191.4	71.8	SND
225	91 347 02 33	32	6.2	307.3	60.8	FLX
				309.5	61.6	DLK
				308.8	61.9	USK
				310.0	62.6	TSD
				310.3	63.4	RAY
				308.5	61.3	HLB
				309.3	61.8	SND
				311.6	64.7	GRY
226	91 347 03 24	46	5.1	308.7	62.0	USK
				309.2	61.9	SND
				308.4	61.4	HLB
				311.5	64.8	GRY
228	91 347 05 45	33	6.0	307.3	60.9	FLX
				309.5	61.6	DLK
				308.8	62.0	USK
				310.0	62.7	TSD
				310.3	63.5	RAY
				308.6	61.4	HLB
				309.3	61.9	SND
				311.6	64.8	GRY
229	91 347 08 00	33	5.5	308.5	62.0	USK
				310.0	63.5	RAY
				309.2	61.7	DLK
				308.2	61.4	HLB
				309.0	61.9	SND

No.	Origin time Y.D.h.m.	Depth (km)	M	BAZ°	Δ°	Station names
232	91 347 18 59	52	6.2	307.2	60.8	FLX
				309.4	61.5	DLK
				308.8	61.9	USK
				309.9	62.6	TSD
				310.2	63.4	RAY
				308.4	61.3	HLB
				309.2	61.8	SND
				311.5	64.6	GRY
234	91 347 19 55	47	5.8	309.6	61.8	DLK
				308.9	62.1	USK
				307.4	61.0	FLX
				310.1	62.8	TSD
				310.4	63.6	RAY
				308.6	61.6	HLB
				309.4	62.1	SND
237	91 348 00 07	211	5.0	145.7	82.4	TSD
				143.5	82.7	USK
				140.7	83.3	FLX
				145.1	83.2	SND
				143.8	83.5	HLB
241	91 349 18 56	102	5.6	146.5	74.7	RAY
				144.8	76.1	USK
				141.8	76.6	FLX
				148.1	73.5	GRY
				146.6	76.6	SND
				145.2	76.9	HLB
242	91 349 21 47	47	5.1	306.8	60.8	FLX
				308.4	62.0	USK
				309.9	63.5	RAY
				308.1	61.4	HLB
243	91 350 04 47	38	5.3	311.0	52.9	USK
				310.5	52.3	HLB
				311.1	52.8	SND

No.	Origin time Y.D.h.m.	Depth (km)	M	BAZ°	Δ°	Station names
245	91 351 04 23	59	5.3	310.7	66.6	USK
				311.3	66.4	SND
				313.4	69.3	GRY
246	91 351 06 38	149	5.9	308.8	59.6	FLX
				310.9	60.2	DLK
				310.3	60.6	USK
				311.7	62.2	RAY
				309.9	60.1	HLB
				310.7	60.5	SND
				313.0	63.4	GRY
249	91 353 01 33	43	6.1	307.2	61.3	FLX
				309.5	62.1	DLK
				308.8	62.4	USK
				310.2	63.9	RAY
				308.5	61.8	HLB
				311.6	65.2	GRY
254	91 354 08 35	48	5.7	307.0	61.4	FLX
				308.6	62.5	USK
				310.1	64.0	RAY
255	91 355 22 02	33	5.0	149.9	46.4	RAY
				147.9	47.8	USK
				152.1	45.3	GRY
256	91 356 08 43	26	6.3	307.5	61.1	FLX
				309.8	61.9	DLK
				309.1	62.2	USK
				310.6	63.7	RAY
				308.8	61.7	HLB
				311.9	65.0	GRY
259	91 357 13 10	23	5.9	307.4	60.4	FLX
				309.5	61.2	DLK
				308.9	61.5	USK
				310.4	63.0	RAY
				308.6	60.9	HLB

No.	**Origin time Y.D.h.m.**	**Depth (km)**	**M**	**BAZ°**	**Δ°**	**Station names**
260	91 359 19 23	33	5.5	307.3	60.7	FLX
				308.8	61.8	USK
				310.3	63.3	RAY

APPENDIX D

TABLE D1

List of earthquakes and broadband stations that could be used for receiver function analysis. * - records that have been used in the feasibility study. ? - records of marginal quality for receiver function analysis.

No.	Origin time Y.D.h.m.	Depth (km)	M	BAZ°	Δ°	Station names
5	91 186 10 58	456	5.6	312.4	61.9	FLX
				315.0	63.4	TSD
				313.9	62.8	USK?
7	91 187 12 19	85	6.3	147.5	71.3	TSD
				145.0	71.5	USK
				141.7	72.1	FLX
10	91 190 05 54	101	5.3	146.9	79.4	TSD
				144.7	79.7	USK
				141.7	80.2	FLX
11	91 190 06 53	33	5.5	120.5	41.5	TSD
				117.0	42.5	USK
				112.8	44.0	FLX
25	91 194 12 15	40	5.7	308.2	57.0	FLX
				309.5	58.0	USK
26	91 195 09 09	223	6.4	4.0	91.0	TSD
				2.0	91.8	USK
				359.3	92.6	FLX
36	91 199 11 56	13	5.8	37.0	72.3	TSD
				35.3	73.7	USK?
				33.0	75.5	FLX?
37	91 201 11 48	35	5.7	296.4	33.4	TSD
38	91 205 09 45	33	5.3	23.4	88.0	USK?

No.	Origin time Y.D.h.m.	Depth (km)	M	BAZ°	Δ°	Station names
49	91 215 08 33	16	5.4	315.6	86.0	TSD?
				313.8	85.4	USK?
53	91 218 14 49	34	5.8	310.3	75.2	TSD
				310.3	74.2	DLK
59	91 225 02 11	10	5.3	63.9	38.9	DLK
				61.5	40.2	TSD?
				59.7	41.8	USK?
60	91 226 12 53	229	5.7	289.8	35.2	FLX
				299.0	36.6	USK
				297.0	36.9	DLK
				299.1	37.6	TSD
61	91 226 19 15	33	6.0	261.3	100.4	DLK?
62	91 227 23 27	105	5.4	296.7	36.6	FLX
				297.1	38.0	USK
				295.4	38.4	DLK
				297.4	39.0	TSD
64	91 229 06 18	10	5.1	134.6	50.8	TSD?
79	91 238 10 01	10	5.3	143.4	38.4	TSD?
80	91 238 14 59	45	5.8	308.7	66.8	FLX*
				311.5	67.4	DLK*
				311.8	68.5	TSD*
				310.4	67.8	USK*
84	91 244 06 51	10	5.2	16.8	39.8	DLK?
87	91 246 09 05	10	6.2	189.7	70.2	USK
				192.5	73.2	DLK
88	91 246 11 56	10	5.8	189.7	70.2	USK?
				192.5	73.3	DLK
96	91 258 06 39	10	5.6	192.1	71.2	TSD?
98	91 261 09 48	5	5.7	158.7	38.2	RAY?
				156.2	39.5	USK
				161.8	41.4	DLK?
99	91 262 01 41	37	5.5	309.6	58.0	USK?

No.	Origin time Y.D.h.m.	Depth (km)	M	BAZ°	Δ°	Station names
101	91 264 15 19	33	5.9	242.0	89.1	USK?
				244.4	91.9	DLK?
109	91 273 00 21	580	6.0	240.9	93.8	FLX
119	91 281 03 31	147	6.0	310.3	63.1	USK
132	91 292 04 59	33	5.1	297.3	36.7	TSD?
136	91 292 21 23	19	6.5	358.1	94.7	DLK?
				357.6	96.7	TSD?
				355.5	97.3	USK
153	91 298 10 39	111	5.7	309.7	66.1	FLX*
				312.5	66.5	DLK*
				311.4	67.1	USK*
				312.8	67.7	TSD*
				312.9	68.6	RAY
156	91 299 02 27	193	5.8	295.3	86.1	USK
				297.5	86.5	DLK
				296.9	87.6	RAY
				297.2	87.1	TSD
				292.9	84.5	FLX
173	91 314 08 20	33	5.1	151.3	45.9	TSD?
				153.9	47.5	DLK?
176	91 315 17 46	33	5.5	178.7	34.2	USK?
				182.8	34.9	TSD?
				183.5	37.0	DLK?
177	91 315 22 34	23	5.9	298.8	81.4	FLX
				303.2	82.9	DLK
				301.2	82.7	USK
				302.9	83.6	TSD
				302.7	84.2	RAY
180	91 317 19 20	308	5.4	309.6	77.9	USK?
				311.3	78.6	TSD?
187	91 323 22 28	21	6.5	144.8	51.7	RAY
				143.0	53.2	USK
				147.6	54.4	DLK
				138.8	53.8	FLX

No.	Origin time Y.D.h.m.	Depth (km)	M	BAZ°	Δ°	Station names
191	91 328 03 47	30	5.1	170.0	36.5	TSD
192	91 329 14 15	147	5.3	147.9	66.4	TSD?
195	91 330 10 41	69	5.8	197.6	40.0	FLX
				298.3	41.4	USK
				298.7	42.4	TSD
				300.0	42.9	RAY
198	91 330 19 40	55	6.2	310.0	67.8	FLX*
				312.9	68.3	DLK*
				311.8	68.8	USK*
				313.1	69.5	TSD*
				313.2	70.3	RAY*
199	91 331 05 03	35	5.9	309.6	58.1	DLK?
				309.1	58.4	USK?
				310.1	59.1	TSD?
201	91 332 17 19	14	5.7	21.5	85.8	DLK?
				19 1	89.0	USK?
221	91 345 17 03	10	5.9	186.5	69.1	FLX?
				189.8	70.2	USK?
				192.1	71.2	TSD?
				192.6	73.2	DLK?
225	91 347 02 33	32	6.2	307.3	60.8	FLX*
				309.5	61.6	DLK*
				308.8	61.9	USK*
				310.0	62.6	TSD*
				310.3	63.4	RAY*
228	91 347 05 45	33	6.0	309.5	61.6	DLK?
				308.8	62.0	USK?
				310.0	62.7	TSD?
				310.3	63.5	RAY?
232	91 347 18 59	52	6.2	307.2	60.8	FLX*
				309.4	61.5	DLK*
				308.8	61.9	USK*
				309.9	62.6	TSD*
				310.2	63.4	RAY*

No.	Origin time Y.D.h.m.	Depth (km)	M	BAZ°	Δ°	Station names
234	91 347 19 55	47	5.8	309.6	61.8	DLK?
				308.9	62.1	USK?
				307.4	61.0	FLX?
				310.1	62.8	TSD?
				310.4	63.6	RAY?
241	91 349 18 56	102	5.6	146.5	74.7	RAY?
				144.8	76.1	USK?
				141.8	76.6	FLX?
246	91 351 06 38	149	5.9	308.8	59.6	FLX
				310.9	60.2	DLK
				310.3	60.6	USK
				311.7	62.2	RAY
249	91 353 01 33	43	6.1	307.2	61.3	FLX*
				309.5	62.1	DLK*
				308.8	62.4	USK*
				310.2	63.9	RAY*
254	91 354 08 35	48	5.7	307.0	61.4	FLX
				308.6	62.5	USK
				310.1	64.0	RAY
256	91 356 08 43	26	6.3	307.5	61.1	FLX*
				309.8	61.9	DLK*
				309.1	62.2	USK*
				310.6	63.7	RAY*
259	91 357 13 10	23	5.9	307.4	60.4	FLX
				309.5	61.2	DLK
				308.9	61.5	USK
				310.4	63.0	RAY
260	91 359 19 23	33	5.5	307.3	60.7	FLX?
				308.8	61.8	USK?
				310.3	63.3	RAY?
262	91 360 11 35	30	5.7	312.4	52.2	RAY?